https://ntrs.nasa.gov/search.jsp?R=19860005753 2020-03-20T16:43:11+00:00Z

NASA TM-88179

NASA Technical Memorandum 88179

Airborne Astronomy Program
Medium Altitude Missions Branch
Preprint Series 033

NASA-TM-88179
19860005753

Far Infrared and Submillimeter Brightness Temperatures of the Giant Planets

R.H. Hildebrand, R.R. Loewenstein,
D.A. Harper, G.S. Orton,
Jocelyn Keene, and
S.E. Whitcomb

LIBRARY COPY

DEC 23 1985

LANGLEY RESEARCH CENTER
LIBRARY, NASA
HAMPTON, VIRGINIA

November 1985

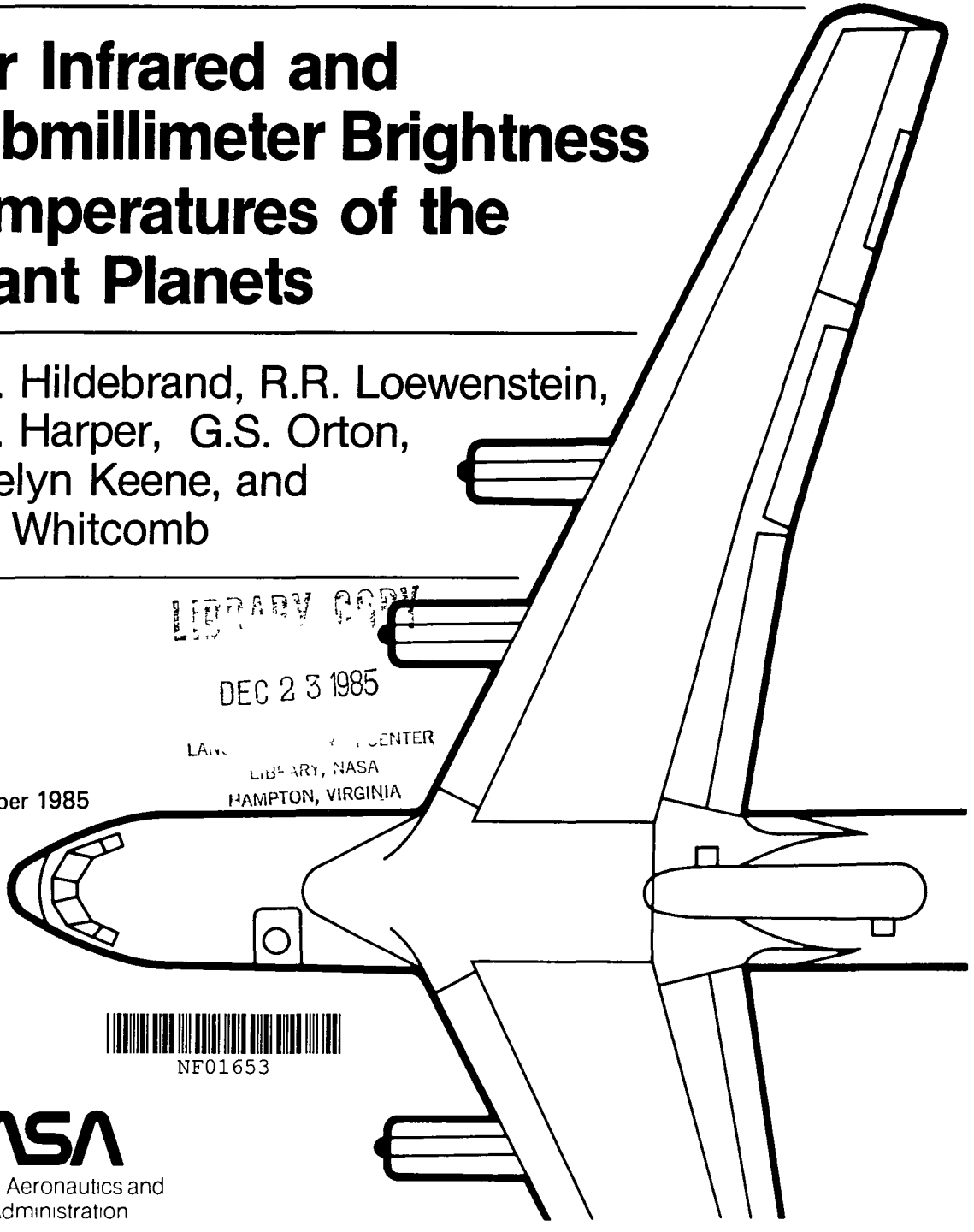

NF01653

National Aeronautics and
Space Administration

NASA Technical Memorandum 88179

Airborne Astronomy Program
Medium Altitude Missions Branch
Preprint Series 033

Far Infrared and Submillimeter Brightness Temperatures of the Giant Planets

R. H. Hildebrand,
R. F. Loewenstein,
D. A. Harper, Ames Research Center, Moffett Field, California
G. S. Orton, Jet Propulsion Laboratory, Pasadena, California
Jocelyn Keene,
S. E. Whitcomb, Ames Research Center, Moffett Field, California

November 1985

NASA
National Aeronautics and
Space Administration

Ames Research Center
Moffett Field California 94035

N86-15223 #

FAR INFRARED AND SUBMILLIMETER BRIGHTNESS TEMPERATURES OF THE GIANT PLANETS

R. H. Hildebrand[1,2,3]

R. F. Loewenstein[1,2,4]

D. A. Harper[1,2,4]

G. S. Orton[5]

Jocelyn Keene[1,2,6]

and

S. E. Whitcomb[1,2,6]

[1]Guest Observer: G. P. Kuiper Airborne Observatory, Ames Research Center, Moffett Field, CA 94035.

[2]Visiting Astronomer at the Infrared Telescope Facility, which is operated by the University of Hawaii under contract from the National Aeronautics and Space Administration.

[3]Enrico Fermi Institute, Department of Astronomy and Astrophysics, and Department of Physics, The University of Chicago, Chicago, IL 60637.

[4]Yerkes Observatory and Department of Astronomy and Astrophysics, The University of Chicago, Williams Bay, WI 53191.

[5]Jet Propulsion Laboratory, California Institute of Technology, 4800 Oak Grove Drive, Pasadena, CA 91109.

[6]Division of Physics, Mathematics, and Astronomy, California Institute of Technology, Pasadena, CA 91125.

ABSTRACT

We have measured the brightness temperatures of Jupiter, Saturn, Uranus, and Neptune in the range 35- to 1000-μm. The effective temperatures derived from the measurements, supplemented by shorter wavelength Voyager data for Jupiter and Saturn, are 126.8 ± 4.5 K, 93.4 ± 3.3 K, 58.3 ± 2.0 K, and 60.3 ± 2.0 K respectively. We discuss the implications of the measurements for bolometric output and for atmospheric structure and composition. The temperature spectrum of Jupiter shows a strong peak at ~ 350 μm followed by a deep valley at ~ 450- to 500-μm. Spectra derived from model atmospheres qualitatively reproduce these features but do not fit the data closely.

I. INTRODUCTION

Far-infrared and submillimeter photometric observations of the giant planets have three principal types of applications: first, the investigation of internal sources of energy; second, the investigation of planetary atmospheres; and third, the establishment of convenient reference objects for photometry of other sources.

The first direct measurements of the bolometric fluxes from Jupiter and Saturn were the 1- to 300-μm airborne observations made by Aumann, et al. (1969). They found that both planets emit substantially more power than they receive from the sun. However, the accuracy of the data was limited by uncertainties in the atmospheric transmission and instrumental response function over the very broad passband and the fact that the spectra of the planets were very different from the spectra of the cool stars used as calibration sources. Subsequent improvements in detectors and far infrared filters allowed measurements in narrower passbands and observations of Uranus (Loewenstein et al. 1977a) and Neptune (Fazio et al. (1976); Loewenstein et al. 1977b. Development of techniques for ground-based observations at submillimeter wavelengths permitted additional measurements between 300 μm and 1000 μm (Loewenstein et al. 1977a; Whitcomb et al. 1979). Most of this subsequent work has been calibrated using the thermal model for Mars derived by Neugebauer et al. (1971) from Mariner data and elaborated and extended by Wright (1976), Wright and Odenwald (1980), and Simpson et al. (1981).

The IRIS experiment on Voyager has provided absolute spectrophotometry at wavelengths of 4.5- to 50-μm of Jupiter (Hanel et

al. 1979) and Saturn (Hanel et al. 1982). Erickson et al. (1978) made spectroscopic observations of Jupiter at $\lambda < 100\ \mu m$. However, their data were calibrated against the moon, requiring a difficult correction for flux into the extended wings of their beam.

The measurements presented here cover the range from 35- to 1000- μm in relatively narrow bands. Roughly 50% of the total flux emitted by Jupiter, 65% by Saturn, and 92% by Uranus and Neptune falls within this range. The airborne (35- to 330- μm) and ground-based (350- to 970- μm) observations were made at approximately the same times, during a period in which Saturn's rings were nearly edge-on as seen from the earth.

The opacities of the atmospheres of the giant planets at far infrared and submillimeter wavelengths come primarily from featureless, pressure-induced absorption in H_2. Their atmospheres are probed to increasing depths by observations at increasing wavelengths. Although it is theoretically possible to derive information about the mixing ratios of H_2, He and CH_4 from far infrared brightness temperatures, the required accuracies are probably greater than permitted by our current data and absolute calibration. However, trace constituents (particularly ammonia in Jupiter) may produce spectral features which are distinguishable by their effect on the shape of the spectra over limited wavelength intervals.

In the following sections we present the observations and instrumentation (II); the data reduction, including corrections, calibration, and planetary radii (III); the results (IV); discussion of

models of the individual planets (V); and a summary (VI). Certain details of the analysis are presented in appendices.

II. OBSERVATIONS AND INSTRUMENTATION

The observations were made in ten or more wavelength bands between 35 μm and 970 μm for each planet. The observations at $\lambda \geq 350\,\mu$m were made at the 3-m NASA Infrared Telescope Facility (IRTF) of the Mauna Kea Observatory; those at $\lambda < 350\,\mu$m were made with the Kuiper Airborne Observatory (KAO). The observations extended over the period 1979 November to 1983 June. All the observations of Saturn were made between 1979 November 27 and 1980 May 7 when the ring inclination to earth was $< 1.^{\circ}7$.

(a) IRTF

The IRTF data were obtained in approximately 330 individual observations during the period 1979 November to 1981 March. Flux densities were obtained in six wavelength bands from 350- to 1000-μm using the University of Chicago Submillimeter/Millimeter Photometer (Whitcomb, et al. 1980). The signals were obtained by repetitive beam switching with a beam separation of 300 arc sec.

Figure 1 shows the transmission curves of the filters as measured on a Fourier transform spectrometer. The apertures were 60 mm for the 1 mm filter (M2) and 29 mm for all submillimeter filters. (Plate scale = 2"/mm).

The measurements with the various submillimeter filters were made in a regular sequence designed to reduce errors due to changes in air mass. The sequence is described in Appendix C.

(b) KAO

The airborne observations were made on the 91-cm telescope of the KAO during the period 1980 January to 1983 June. Four different helium cooled photometers were used: photometers G1, S1, and H1 each contained a single detector and photometer G2 consisted of a close packed hexagonal array of seven detectors (one central detector surrounded by six). Filter passbands are shown in Figure 2. The filters in photometers G1 and G2 were identical and included both bandpass and long-wavelength pass filters. Filters G1-5, G1-6, G2-5 and G2-6 have short wavelength leaks of a few percent or less between 20 μm and 50 μm. These leaks require corrections up to 15% in flux ratios when comparing objects of significantly different temperatures. For many of the observations, we were able to switch in additional Teflon or Calcium Flouride blocking filters which rendered the leaks completely negligible. (See footnotes (f) and (g) of Table IV for specific notes on filters.)

The two water radiometers on board the KAO are described by Kuhn et al. (1976). For specific notes on the water vapor measurements during the airborne observations, refer to footnote (a) of Table IV. The dependence of the atmospheric transmission function upon the line of sight water vapor was calculated by Stier (1983 - private communication) based upon the model of Traub and Stier (1976).

III. DATA REDUCTION

(a) Corrections, Analysis

The signals have been corrected for partial resolution of the

planetary disks (Appendix A), for shadowing of Saturn's disk by the rings (Appendix B), and for atmospheric transmission and the spectral response of the photometers (Appendixes C, D). The correction for partial resolution does not include the effect of limb darkening; the effect of this simplification is estimated in Appendix A. Because the ring inclination was less than 1.7° for all observations, no correction is made for emission from Saturn's rings.

For the IRTF data, all signals are corrected to the same values of the line of sight water vapor, w, before taking ratios of unknown to calibration signals (w = 1 mm H_2O for submillimeter measurements, 5 mm H_2O for millimeter measurements; see Appendix D). For the KAO data the atmospheric corrections of individual measurements were much lower. The spectra of the unknown and calibration sources were assumed to be similar in gross features for $\lambda \gtrsim 350\ \mu m$, but the source spectra of cold and warm planets (e.g. Neptune and Mars) were not similar even in their gross features for $\lambda \ll 100\ \mu m$. It was therefore necessary to use different analysis procedures for the IRTF and KAO data. See Appendix D for a description of the IRTF data reduction and Loewenstein et al. (1977a) for the KAO procedure.

(b) Effective Wavelength

The detection efficiency at frequency ν with line of sight water vapor w depends on the atmospheric transmission, $T(\nu,w)$ and on the spectral response of the photometer $A(\nu)$. For a source with spectrum $S(\nu)$, we define a flux weighted mean frequency for the i^{th} filter to be

$$\langle \nu_{iw} \rangle \equiv \int_0^\infty \nu\, S(\nu)\, A_i(\nu)\, T(\nu,w)\, d\nu \Big/ \int_0^\infty S(\nu)\, A_i(\nu)\, T(\nu,w)\, d\nu$$

The wavelengths shown in the tables and figures are those corresponding

to the mean frequencies so defined (i.e. $\lambda_i = c/\langle\nu\rangle_i$).

(c) Brightness Ratios

Brightness ratios are calculated from the signal ratios using the planet radii discussed in Section IIIe after corrections for partial resolution of the disk and the inclination of the planet pole.

(d) Calibration: Mars Model

Temperatures are derived from the brightness ratios using Mars as the primary calibration object. The Mars temperatures are based on the model of Neugebauer et al. (1971) as extended by Wright (1976) and further extended and tabulated by Wright and Odenwald (1980) and Odenwald (1984-private communication). The model predicts a decline in brightness temperature as the wavelength increases. We have assumed $T(\lambda > 350\ \mu m) = T(\lambda = 350\ \mu m)$. The errors shown in the tables do not include any estimate of the uncertainty in the model.

We do not attempt to evaluate the accuracy of the Wright/Odenwald model. We have, however, compared that model with the more detailed model of Simpson et al. (1981). For the times of the observations, the Mars temperatures of the two models were very nearly equal for $\lambda < 80\ \mu m$. The discrepencies are smaller than the errors we estimate for the measurements. At increasing wavelengths the temperatures of the Simpson model decrease less rapidly than those of the Wright/Odenwald model with a discrepency of ~ 7 K at 300 μm. We have assumed the Wright/Odenwald model because it is more easily generated for a given epoch and because it has been widely used as a standard. We have attempted to give sufficient data in the accompanying tables to allow

re-calibration when better reference models are available.

(e) Planetary Radii

Published direct observations of planetary radii have been made at different wavelengths for the different planets and hence correspond to different depths in the atmospheres. The discrepencies are of order one percent in radius. For consistency, we use radii computed for 1 bar pressure levels which should be approximately the mean radii for the far IR and SMM emission.

For Jupiter, we use the 100-mbar values R_{eq} = 71541 ± 4 km and R_{pol} = 66896 ± 4 km of Lindal et al. (1981). These values were adjusted to the 1-bar level (Z = 46 km) with a mean of the Lindal et al. models (e.g. the nominal model given by Orton, 1981). For Saturn, we use the 182.2-mbar radius, R_{eq} = 60309.5 km, and ellipticity, ϵ = 0.096, of Kliore et al. (1980) adjusted to the 1-bar level (Z = 76.6 km) with a model approximating the preliminary results of Tyler et al. (1982). For Uranus, we use the 8 x 10^{13} cm^{-3} (approximately 1 μ-bar) values R_{eq} = 26156 ± 30 km and ϵ = 0.024 ± 0.003 given by Elliott et al. (1981). The adjustment to the 1-bar level (Z = 582 km) is based on the models of Tokunaga et al. (1983). For Neptune, we use the 4 x 10^{13} cm^{-3} values R_{eq} = 25225 ± 30 km and ϵ = 0.021 ± 0.004 given by Elliot (1979), adjusted to the 1-bar level (Z = 465 km), again on the basis of the atmospheric models of Tokunaga et al. (1983). These atmospheric models for Uranus and Neptune, while constrained by recent infrared data in the 20 μm-region, imply altitude adjustments close to those derived from the equilibrium models of Appleby (1980) or Wallace (1980). The largest uncertainty in the radius adjustments for Uranus and Neptune stems from the

uncertainty in the mean molecular weight. We assume a bulk composition of 90% H_2 and 10% He, consistent with the stellar occultation analyses. There are no firm observational constraints on the bulk compositions of Uranus or Neptune. A 10% change in the He mixing ratio translates into a change in the radius adjustment of approximately 50 km.

With these adjustments, we obtain the assumed 1-bar radii listed in Table I.

For Mars, we use the triaxial ellipsoid fit of Sweetnam, (1980) with a polar radius 3377.1 km and equatorial components 3393.5 km and 3400.0 km. We use $R_{eq} = (3393.5 \times 3400.0)^{1/2} = 3397$ km.

The effective semi-diameters of the planets, $\bar{\varphi}$, shown in Tables II - IV, are computed from the radii in Table I taking into account the inclinations of the planet poles to the line of sight on the dates of the observations. The range of angles during the observations is shown for each planet in the last column of Table I. The pole coordinates are based on the report of Davies et al. (1980) as presented in the 1982 Astronomical Almanac.

(f) Effective Temperatures

The effective temperatures of the planets shown in Table VI were calculated by integrating the solid curve spectra in Figures 3-6 (see next section). The value obtained gave the emitted power (E) within the 30- to 1000- μm range, Except for Jupiter, power short of 30 μm was included by first estimating the temperature of the planet and calculating the correction assuming the spectral shape to be

represented by a blackbody. The temperature is then given by $T_{eff} = (\Xi/\sigma)^{1/4}$. Jupiter's spectrum short of 30 μm was taken from Hanel et al. (1979) and combined with the Figure 3 data.

IV. RESULTS

The journals of the observations are given in three separate parts: Broadband IRTF observations (Table II), Narrower band IRTF observations (Table III), and KAO observations (Table IV). The brightness temperature measurements are combined and summarized in Table V. Since these are not narrow band measurements the power detected depends in part on the shape of the spectrum which is not known a priori. We therefore use semi-empirical models to estimate the shape and hence to adjust the flux densities. The combined results are plotted in Figures 3 - 6 together with curves representing adjustments of the semi-empirical models fitted to the data. The original models for Jupiter and Saturn are based on those of the Voyager IRIS team (e.g. Hanel et al. 1979; 1982) extrapolated from data taken for λ <50 μm; the models for Uranus and Neptune are those of Tokunaga et al. (1983). The data were first reduced using these original models (dashed curves). The deviations of the reduced data points from the assumed curve were fitted by a smooth function that was then used to adjust the original model to minimize the deviations. When necessary, this new source curve was then used to re-reduce the original ratios following the procedure described in the appendix of Jaffe et al (1984). This procedure required two iterations for Jupiter, one for Saturn and Uranus, and none for Neptune. The final curves are shown in the figures (solid curves). The plotted points have been derived assuming the spectral shape of these

adjusted curves. It should be stressed that these curves are not unique, but represent only plausible spectra containing spectral features predicted by the atmospheric models. The adjusted models give consistent results when each of the giant planets is used in turn to replace Mars as the standard. This is a necessary condition for any valid set of models.

The number of integrations used in measuring the airborne points was usually too small to permit estimates of statistical errors for individual points. Where errors could be estimated, they are shown in Table IV. Since all airborne measurements are shown in Figures 3-6, the spread can be used to judge the extent of systematic errors. The principal known sources of systematic errors for these points are uncertainties in atmospheric water vapor (airborne data) and uncertainty in the Mars model (all data). We emphasize that none of the errors shown in the tables include the uncertainty in the Mars reference temperatures. We assume an absolute accuracy of ± 15% in flux. The averages and statistical errors of the combined data points are tabulated in Table V. The average of the airborne statistical errors is 1.5 K and represents the average statistical error in any given airborne measurement.

We have plotted the individual airborne flux densities and the combined groundbased flux densities for each planet in Figures 7 and 8, normalized to a fixed planetary solid angle. This representation affords a better feeling for the significance of the various observational errors.

Recent measurements by Oregon/Queen Mary College Group (O/QMCG, Orton, et al. 1985) in the range 350 μm to 3.3 mm are generally in satisfactory agreement with our data, but somewhat lower. The difference is due in part

to differences in assumed Mars reference temperatures. The principal discrepancy is in the Jupiter data in the region 350- to 500-μm, where our points are higher and show a strong peak at ~350 μm followed by a valley at ~450 μm. This feature first appeared in measurements with filters CH3 (353 μm), CH2 (414 μm), NO4 (517 μm), and CH5 (664 μm). Although it appeared in each of three series of measurements on the first night of the observations, we decided to repeat the observations on the following night. Again the feature appeared in Jupiter's spectrum (but not in those of other planets) in each of three series of measurements.

For all of those measurements the lowest measured point was that for the cut-on filter NO4 (517 μm). Since the effective wavelength for that filter depended strongly on the relative atmospheric transmission in the 450, 650, and 750 μm atmospheric windows, we replaced it in later runs with CH4 (450 μm), a relatively narrow band filter with a shorter effective wavelength. The effect was then even more pronounced (two series of measurements on each of two nights).

In view of this sequence of observations and the fact that only Jupiter shows the effect we are confident that it is real. We emphasize, however, that a determination of the exact magnitude of the effect and the exact position of the minimum will require new measurements with narrower band filters. For the filters used in these observations, the results of the iterative procedure used to derive the flux densities from the signals depend strongly on the spectral response, including atmospheric effects, in regions where the brightness temperature of the source changes rapidly with wavelength.

The strong dependence on spectral response may explain or contribute to the discrepancy between our results for Jupiter and those of the O/QMCG which do not show the same structure near 400 μm. We emphasize however, that the results are generally in good agreement. Evidently, this portion of Jupiter's spectrum should be re-examined with narrower passbands.

Integrating the curves in Figures 7 and 8 and correcting for unmeasured flux shortward of 35 μm, one derives the effective temperatures given in Table VI. E/A is the ratio of emitted to absorbed radiation.

V. DISCUSSION

The 30- to 1000-μm spectral range covered by our data contains approximately 50% of the total flux from Jupiter, 65% from Saturn, 92% from Uranus, and 92% from Neptune. We are therefore able -- especially for Uranus and Neptune -- to reduce considerably the uncertainties in determining the effective temperatures. The implications of these temperatures for internal energy sources are discussed later in this section (§V B).

First, however, we discuss the predictions of a number of theoretical atmospheric models, the details of which are presented in Appendix E. The model spectra are useful as first-order approximations in the reduction of signal ratios to brightness temperatures, as in Section IV, and for extrapolating to wavelengths not actually observed (e.g., when estimating effective temperatures). Such extrapolations (specifically, from the 30- to 50-μm region in which Voyager data on Jupiter and Saturn may be used as alternatives to the absolute

calibration based on Mariner measurements of Mars) can also provide a consistency check on our absolute calibration system. Finally, comparing predicted spectra with observed fluxes allows us to test the plausibility of certain assumptions about temperature profiles, mixing ratios, and cloud structure.

A. Comparisons with Atmospheric Models

The Voyager IRIS experiment has obtained many absolutely-calibrated spectra of Jupiter, including some observations of the whole disk, out to a wavelength of 50 μm (Hanel et al. 1979). The theoretical curves displayed in Figures 9-11 are all consistent with the Voyager results (Orton et al. 1982b). The agreement of the Voyager and KAO fluxes provides an independent check on the absolute calibration in the 30- to 50- μm region. Figure 9 includes the spectrum of a model atmosphere without NH_3 ice clouds and one with NH_3 clouds having a characteristic particle scale height (H_p) equal to 0.15 times the scale height of the gas H_g). Figures 10 and 11 show spectra resulting from similar clouds with particle scale heights equal to 0.50 and 0.05 times the gaseous scale height, respectively. The models are extensions of those presented by Orton et al. (1982b). Although they predict that the presence of NH_3 ice particles will decrease the brightness temperature between 300 μm and 500 μm, none matches the shape of the observed spectrum in detail. Hence, although the data suggest the presence of some source of gaseous opacity in Jupiter's atmosphere which is not prominent in the atmospheres of the other giant planets, determining its nature may require additional observations (in particular, measurements at higher spectral resolution which permit

more accurate correction for telluric absorption) and refinements in the theoretical models. (See discussion in §IV.)

Figure 12 shows spectra of models for Saturn with a PH_3 mixing ratio of 1.5×10^{-6} in the deep atmosphere, following the results of earlier investigations (see Appendix E). Models with larger mixing ratios have been included to show the influence of PH_3 lines in this region of the spectrum. The measurements at 204.3, 221.1, and 328.9 μm all appear to lie below the model spectra and could be interpreted as indicating that larger mixing ratios are required or that there is an unmodeled absorber. Since the model spectra in Fig. 12 provide satisfactory fits to the data throughout most of the far infrared, we conclude that the global average of the optical depths of the clouds cannot be as high as the values suggested by Orton (1983) for clouds near the equator and near 15° S. latitude. The average depth may be reduced by relatively bright "clear" regions in the northern hemisphere (Pirraglia *et al.* 1981; Gautier *et al.* 1983).

Models based on the Uranian temperature profile of Tokunaga *et al.* (1983, shown here in Fig. 13) give a reasonable fit to our data. The differences in the temperature near and below the 1-bar pressure level are a direct consequence of various assumptions about the mixing ratio of CH_4 in the deep atmosphere (see Appendix E). The submillimeter fluxes are sensitive to the CH_3 mixing ratio because of the pronounced effects of the latent heat of condensation on the adiabat for large abundances.

The temperature structure assumed for Neptune (Fig. 15) resulted from perturbing the models which Tokunaga *et al.* (1983) based on the

results of Appleby (1980), in order to achieve the best fit to our data. The required temperatures at the 300- to 500- μm bar level are one to two degrees cooler than assumed by Tokunaga et al. Among the model spectra shown in Figure 14 and Figure 16, the ones with the lowest CH_4 abundance provide the best fit to the observations across the entire spectral range (although this statement is based almost exclusively on the single data point at 960 μm in the case of Neptune). Data from the O/QMCG will provide additional constraints near 1 mm. Our submillimeter data suggest a [C]/[H] elemental abundance ratio near or below Jovian or solar values (Orton, et al. 1985). The models provide satisfactory fits to the 17.8 μm and 19.6 μm data of Tokunaga et al. (1983). All of the model temperatures are cooler than those given by the observations of Orton et al. (1983) at 10.3, 11.6, and 12.5 μm, which is consistent with their interpretation that part of the flux in this spectral region is reflected sunlight. The greatest difficulty associated with the Uranus and Neptune models is the divergence between the high brightness temperatures which they predict at 3mm (for low CH_4 abundances) and the much lower observed temperatures (e.g., Ulich 1981) which would appear to be better matched by the 2% CH_4 model. This is, of course, the spectral region for which the Martian brightness temperatures upon which the absolute calibration of the submillimeter photometry is based are most uncertain. However, the 960 μm fluxes for Jupiter and Saturn are not excessively high.

B. Effective Temperatures

The thermal energy fluxes of Jupiter and Saturn due to internal

sources of heat are equal to 1.8 and 1.7 times the solar input, lower than previous values. The decrease is due to the use of more recent estimates of the Bond albedos (see Table VI). For Jupiter, the value is consistent with an interpretation in which all of the excess power is supplied by gravitational contraction and heat stored from the original contraction of the planet from the solar nebula (Graboske et al. 1975; Bodenheimer et al. 1980). Saturn, however, requires an additional source of energy which can most plausibly be provided by differentiation of helium within the interior (e.g. Stevenson 1980).

The effective temperature which we derive for Uranus is similar to the previous estimates by Fazio et al. (1976), Loewenstein et al. (1977b), and Stier et al. (1978). There is no indication of a change over this period of time. Lockwood et al. (1983) have derived Bond albedos of 0.342±0.032 for the 1962 epoch and 0.393±0.037 for the 1981 epoch. From these values, one would predict equilibrium temperatures of 57.0±0.8 K and 55.8±1.0 K, respectively. Recent preliminary work has been done to remeasure the geometric albedo (Neff et al. 1984). This work extends measurements of the phase function of the planetary disk to high angles via the Voyager spacecraft Imaging Subsystem experiment (Wenkert et al. 1984), and combines these with atmospheric cloud models which provide reasonable extrapolations to high phase angles in the full spectral range of relevance (Pollack et al. 1984). The derived Bond albedo is in the range 0.31 and 0.42, implying an equilibrium temperature of 56.4±1.2 K. There is sufficient overlap in the uncertainties of absorbed and emitted energy to support the absence of an internal heat source or one as large as 40% of the absorbed solar

energy.

Our new effective temperature for Neptune (60.3±2.0 K) is larger than the earlier values of Loewenstein et al. (1977b; 55.5±2.3 K) and Stier et al. (1978; 58.5±2 K). Newburn and Gulkis (1973) suggest a Bond albedo for Neptune which is approximately the same as for Uranus, based on the similarity of their spectra. Murphy and Trafton (1974) recommend a similar value. Albedos of 0.33 or 0.34 imply an equilibrium temperature of about 45 K. As in the case of Uranus, more recent preliminary work has been done on the geometric albedo (Neff et al. 1984), but only limited observations have been made of the phase function (Wenkert et al. 1984). As of this writing atmospheric cloud models (Pollack et al. 1984) are still very primative. Assuming the same phase integral as for Uranus, we estimate the Bond albedo of Neptune to be about 0.29, implying an effective temperature of 46.4 K. The uncertainty is probably about the same as for the temperature of Uranus. Our data thus imply an internal power source for Neptune approximately 2.8 times larger than the absorbed solar flux. Although this value is significantly larger than the limit for Uranus, Hubbard and MacFarlane (1980) have pointed out that it is still less than expected on the basis of homogeneous cooling from an initial hot state, and they postulate that the available fossil heat was reduced during its evolutionary history by upward redistribution of heavier materials.

VI. SUMMARY

We have presented new photometric data on the giant planets covering the range 30- to 1000- μm. The data permit a more accurate

determinations of effective temperatures than earlier studies with broader filters, more limited data sets, and less complete spectral coverage. Our results are generally consistent with previous work, and major conclusions regarding internal heat sources are unchanged.

It is relatively easy to fit a range of reasonable atmospheric models to our data in the 30- to 100- μm wavelength range. Fluxes at longer wavelengths are sensitive to a number of parameters, such as the presence of NH_3 ice particles in Jupiter's atmosphere and the CH_4 mixing ratio in Uranus and Neptune, but to discriminate between models, from moderate-bandwidth photometry would require accurate absolute calibration. Since no direct absolute calibration is available in the 100- to 1000- μm spectral range, any conclusions about atmospheric structure from current submillimeter data should be regarded as tentative. With that caveat, we can make the following observations:

(1) Our data indicate the presence in Jupiter's spectrum of excess emission (compared to theoretical models) at 300-400 μm, followed by a pronounced dip at ~500 μm. Additional measurements with higher spectral resolution would be desireable. The observations of the O/QMCG will provide additional data in the SMM region and will extend to longer wavelengths.

(2) There is slightly less flux observed from Saturn at ~200 μm than predicted by our atmospheric models, suggesting the possible presence of an unmodelled absorber.

(3) The submillimeter fluxes from Uranus and Neptune seem most consistent with low mixing ratios (<1%) of CH_4 in their deep

atmospheres.

ACKNOWLEDGEMENTS

We thank the staffs of the IRTF and KAO for their assistance during the observations. This work was supported by NASA grants NSG-2057, NAG-W-4, and NGR 14-001-227. RHH and RFL wish to thank J. Simpson and M. Stier for additional Mars modeling; Harvey Moseley and the Oregon/Queen Mary College Group for allowing us to use unpublished data; and the staff and crew of the KAO for their usual superb help. We are grateful to Ira Nolt for comments on a draft of the manuscript.

GSO acknowledges support from the Galileo Project and from the Planetary Atmospheres Program of the NASA Office of Space Sciences and Applications for work carried out under NASA contract NAS 7-100 at the Jet Propulsion Laboratory, California Institute of Technology. We thank J. Hansen, N. Habra and D. Soll at the NASA Goddard Institute for Space Studies for computing support; G. Birnbaum and C. Chapodos for laboratory results in advance of publication; and J. Appleby, K. Baines, J. Bergstralh, S. Gulkis, M. Klein and T. Thompson for useful advice relevant to this work.

APPENDIX A

Partial Resolution of the Planetary Disk

In some cases, especially the observations of Jupiter, the angular radius of the planet is appreciable in comparison with the beam radius. It is therefore necessary to correct the observed signals for partial resolution of the disk, i.e. for a decrease in detection efficiency with increasing displacement from the optic axis. The normalized scans of Mars give the efficiencies, $E(\phi)$, as a function of the displacement, ϕ. To good approximation these scans can be fitted by gaussians. For a planet of angular radius $\bar{\Phi}$ in which the brightness is a function $b(\alpha)$ of the emission angle $\alpha = \arcsin(\phi/\bar{\Phi})$, the disk correction is

$$D(\bar{\Phi}) = \int_0^{\bar{\Phi}} b(\alpha)\pi\phi\, d\phi \Big/ \int_0^{\bar{\Phi}} E(\phi)b(\alpha)\pi\phi\, d\phi . \qquad (A1).$$

i.e., if S = observed signal, then $D(\bar{\Phi})S$ = signal which would be observed for a planet of the same luminosity and the same $b(\alpha)$, but with $\bar{\Phi} \to 0$.

We have used the assumption $b(\alpha)$ = constant to obtain the corrections shown in Tables II and VI. As an indication of the sensitivity of $D(\bar{\Phi})$ to $b(\alpha)$ we have used the 45 μm (Pioneer 10 and 11) values of $b(\alpha)$ determined for Jupiter by Ingersoll et al (1976). We have made fits of smooth curves to their measured values averaged over five zones of latitude. The difference between the corrections for $b(\alpha)$ = constant and for $b(\alpha)$ based on Ingersoll *et al* (1976) is negligible in comparison with our estimate of the error (10%) in $D(\bar{\Phi})-1$ due to uncertainties in $E(\bar{\Phi})$.

APPENDIX B - EFFECT OF SATURNS RINGS

Voyager 2 measured the temperatures of the A and C rings of Saturn to be 69 K and 85 K respectively (Hanel et al, 1982). At the encounter, the ring inclination to the sun was 8°. At the time of our observations the ring inclination angle to the sun was $< \pm 1^{\circ}$. Because of the low inclination we assume that the ring temperature would be significantly less than the temperatures measured by Voyager. In this case, the dominant effect of the rings would be to block the emission from the disk. Since the ring inclination to earth was always less than 1.7° during our observations, the greatest reduction in the effective disk area would be 1.5%. The correction is much lower for $\lambda \geq 300$ μm.

APPENDIX C - SEQUENCE OF GROUND-BASED MEASUREMENTS

The individual observations used in the IRTF investigations followed a regular pattern. Consider, for example, a series of observations of Mars, Jupiter and Saturn using the submillimeter filters CH2 (broadband), and CH3, CH4, CH5 (narrower band). We use M2, J3, etc. to denote observations of Mars with filter CH2, Jupiter with filter CH3, etc. and S(M2), S(M3) etc. to denote the corresponding signals.

A single series would proceed in the order M2, M3, M4, M5, M2, J2, J3, J4, J5, J2, S2, S3, S4, S5, S2, and the entire series would be repeated at least once and usually twice. Note that filter CH2 was used before and after the other filters on each planet. It usually took less than 10 minutes to complete the five successive counts on a single planet. The corresponding change in air mass was usually < 0.05.

Hence corrections for changes in air mass within the set of five counts were almost negligible. In computing ratios of counts such as S(M3)/S(M2) for one series we simply interpolated linearly by air mass between the S(M2) values at the beginning and the end of the series to find a value for the air mass corresponding to M3.

The time between the first and second series for a given planet was approximately 45 minutes. The corresponding change in air mass, typically ~ 0.15, was usually enough to cause a small but measureable change in a signal ratio such as S(M3)/S(M2). Insofar as possible, the observations were timed to give equal air masses for each of the planets when averaged over all observations for one night.

APPENDIX D - ANALYSIS OF IRTF DATA

(1) Broadband Data

The counts obtained with the broadband filters CH2 and MP2 are insensitive to fine structure in the source spectra, they have high statistical accuracy, and they have been repeated often enough to provide well-sampled signal vs. air mass curves. We use these counts to derive brightness ratios for the various planets, and to provide reference points in deriving the shapes of the individual spectra (Section 2).

The steps in the analysis of the broadband data are as follows:

(i) Plot the signals vs. air mass for each planet for each night. Discard all data on nights when the curves indicate a change in water vapor.

(ii) To those plots, fit the water vapor curves to estimate the

zenith water vapor.

(iii) Adjust all the data for a given night to a common line-of-sight water vapor.

(iv) Combine the adjusted values weighting individual counts according to their noise values, using the nominal errors or the mean error, whichever is larger.

(v) Make a Chi-Squared test of the N adjusted values and increase the error of the combined result by $(\chi^2/N)^{1/2}$ if the reduced chi squared is >1.

(vi) Calculate the ratios of the averages <S(J2)>/<S(M2)> etc. where the counts in the denominators are for the reference planet (Mars, or, where necessary, an intermediate standard).

(vii) Multiply the ratios by the disk correction factors shown in Tables II and IV and by the ratios of planetary solid angles to obtain global surface brightness ratios B(J2)/B(M2) etc. For the range of water vapor of these measurements, the brightness ratios for these filters on different nights are in satisfactory agreement and show no dependence on zenith water vapor: the expected result for the broadband data, whatever the fine structure, if overall the planets have roughly Rayleigh-Jeans spectra within the passbands of the filters (as assumed in preparing the water vapor curves).

(viii) Assume a brightness temperature for the reference planet for the date of the observation and calculate a brightness temperature for the "unknown" planet.

(ix) Combine the brightness temperatures for the various nights

with weighting and chi-squared tests as in steps (iv) and (v). We assume no change in giant planet temperatures during the period of the observations. No change is indicated by the results.

(2) Narrower Band Data

In principle, the procedure we have described for the broadband data could be used also to find the signal ratios S(J3)/S(M3) etc. and hence the brightness temperatures for the narrower bands. However, the errors in determining the relative brightnesses in the various passbands for a single planet are reduced by the following procedure:

(i) Calculate $[S(M3)/S(M2)]_w$, $[S(J4)/S(J2)]_w$, etc., where w = line of sight water vapor for a particular measurement of S(M3), S(J4), etc. and $S(M2)_w$, $S(J2)_w$, etc. are the values of the broadband signals interpolated to the same values of w. These ratios are not independent of w; e.g. S3/S2 decreases and S5/S2 increases with increasing w. Typically, the change from one series to the next is 3-10%.

(ii) Adjust the ratios for successive series to a common value, w_o, using empirically determined corrections (linear in w) based on the data for all runs. The ratios thus determined agree within statistics. For the submillimeter data (filters CH2, CH3, N4, CH4, and CH5) we choose w_o = 1 mm. The range of values is $0.3 \leq w \leq 1.5$ mm. For the millimeter data (filters MP2 and MP4) we choose w_o = 5 mm. The range of values is $3.4 \leq w \leq 6.4$ mm.

(iii) Combine the adjusted values to obtain $\langle S(M3)/S(M2)\rangle_w$, $\langle S(J4)/S(J2)\rangle_w$ etc. with weighting and chi-squared tests as discussed in section 1.

(iv) Calculate brightness ratios relative to the calibration object (Mars) using the relationships

$$B(J3)/B(M3) = [B(J2)/B(M2)]/[\langle S(J3)/S(J2)\rangle_w / \langle S(M3)/S(M2)\rangle_w]$$

etc. and using the values of B(J2)/B(M2) etc. as discussed in section 1. Note that if the small adjustments of step (ii) are correct, then the value of w_o will not influence the calculated value of B(J3)/B(M3) etc. The effective wavelength is slightly dependent on w_o but the dependence is much weaker than for the broadband filters.

(v) Calculate brightness temperatures.

APPENDIX E

Details of Atmospheric Models

Synthetic spectra of Jupiter and Saturn were computed from physical models with 10 cm^{-1} wide ("flat") elements centered at 99 through 499 cm^{-1} and 5 cm^{-1} wide elements centered at 34 through 99 cm^{-1} for the airborne observations, and 2.5 cm^{-1} wide elements at 9.0 through 34.0 cm^{-1} for the ground-based observations. This approach allowed absorption features such as the manifolds of NH_3 rotation-inversion lines to be resolved.

The opacity of the Jovian atmosphere is dominated by H_2 and NH_3 in the 40 μm - 1 mm region. The H_2 collision-induced dipole absorption was calculated using recent models derived for a variety of colliding species: H_2-CH_4 according to Dore et al. (1983), H_2-He according to Cohen et al. (1985). Absorption by NH_3 was calculated using direct integration of inversion and rotation-inversion lines whose spectroscopic parameters are summarized by Husson et al. (1982), based on Husson et al. (1981). Additional gaseous absorption by PH_3 and CO was modelled using line parameters given by Hussonet al. (1982).

The radiative transfer calculations were performed using the matrix operator algorithm of Grant and Hunt (1969) in a multiple-layer approximation which used twenty homogeneous layers per decade of pressure change to simulate the gradual change of atmospheric properties with altitude. Direct integration of line absorption was performed using the method of Scott (1974) as modified by Orton (1981).

The temperature structure of Jupiter used in the calculations was adopted from the neutral atmosphere inversion of the Voyager Radio

Subsystem (RSS) occultation experiments (Lindal et al. 1981), assuming respective molar fractions of 89% and 11% for H_2 and He (Gautier et al. 1981). Ammonia was assumed to have a molar mixing ratio of 2.2×10^{-4} in the deep atmosphere (Lindal et al. 1981) with depletion of higher levels owing to saturation equilibrium and photochemical destruction as modelled by Orton et al. (1982a). The vertical distribution of PH_3 was represented by a maximum mixing ratio of 6×10^{-7} with a gradual depletion with altitude above the 1 bar level, following the profile derived by Kunde et al. (1982) from Voyager IRIS spectra. A constant CO mixing ratio of 2.5×10^{-9} was assumed, an average of the approximate results of Beer (1975) and Larson et al. (1978). We note that the influence of PH_3 and CO lines on the spectrum in 10.0 cm^{-1} through 2.5 cm^{-1} resolution elements appeared to be small.

The temperature structure of Saturn used in the calculations was derived from the results of the planet-wide averaged temperature structure determined from the Voyager IRIS data given by Hanel et al. (1983), with temperatures deeper than 350 mbars derived from the preliminary neutral atmosphere inversion of the Voyager IRIS occultation experiment (Tyler et al. 1982) after adjustment of the bulk composition to 93% H_2 and 7% He (Gautier et al. 1983). Ammonia was assumed to have a molar mixing ratio of 2×10^{-4} in the deep atmosphere. An alternative value of 5×10^{-4} was tested, following models limits given by Klein et al (1978), and was found to affect our spectra negligibly. Depletion of NH_3 at high levels followed saturation equilibrium. A simple model for the vertical distribution

of PH_3 was used: a constant mixing ratio of 1.5×10^{-6}, roughly consistent with the results of Tokunaga et al. (1980) and Courtin et al. (1981), with a cutoff near the base of the stratosphere. We discovered that the presence or absence of stratospheric PH_3 was not significant for our calculations. For consistency with Jupiter, we assumed a constant CO mixing ratio of 2.5×10^{-9}, although its influence on our calculations of the Saturnian spectrum was extremely small, (as was the case for Jupiter.)

We also tested various physical models for NH_3 ice clouds in the Jovian atmosphere following the general scheme used by Orton et al. (1982b). The particles are characterized by a mode radius which is left a free parameter, a 10% variance in the particle size distribution, and a scattering phase function taken from fitting the NH_3 particle phase function observed in the laboratory with visible light (Holmes, 1981; Holmes et al., 1980) using the Pollack and Cuzzi (1980) semi-empirical algorithm for irregularly-shaped particles. No cloud particles were assumed higher than the 100-mbar temperature minimum or deeper than the 630-mbar saturation level. The vertical distribution was parameterized by particle scale height to gas scale height ratios, H_p/H_g, of 0.50, 0.15 and 0.05. Indices of refraction for NH_3 ice were taken from Martonchik et al. (1983) which are based primarily on the absorption measurements of Sill et al. (1980). For very low frequencies absorption was extrapolated exponentially downward with decreasing frequency, consistent with the lowest available frequency measurements of Sill et al. This treatment ignores possible phonon absorptions, such as occur in water ice (e.g. Mishima et al.,

1983), owing to the absence of relevant laboratory data. Other restrictions on the particle size and vertical scale height determined by Orton et al. (1982b) were also observed. As discussed in the main text, physical models for clouds in the Saturnian atmosphere were not invoked.

The 35- to 100-μm spectra of Uranus and Neptune are expected to be dominated by the collision-induced absorption of H_2, and the comparison with model spectra tend to support this view. At this time, there is no evidence to suggest that non-continuous features should be present in the spectrum. For Uranus (and Neptune) the low temperatures eliminate NH_3 at detectable levels, unless present in abundances exceeding saturation equilibrium by many orders of magnitude. Phosphene should also be depleted by saturation equilibrium, although not as much as ammonia. Although carbon monoxide may not be depleted by a similar process, its influence on the measurements should be very small if its mixing ratios in Uranus and Neptune are similar to Jupiter. We therefore assumed that the spectrum could be described well by the continuum due to H_2. Thus, direct comparisons between the computed spectrum and the brightness temperatures given in Table II at various wavelengths are physically meaningful.

For the temperature structures for Uranus and Neptune, we followed a procedure adopted by Orton et al. (1983) which examines existing models by Tokunaga et al. (1982). Their temperature structures are partially based on radiative-convective equilibrium models of Appleby (1980) and are constrained to match 17.8 and 19.6 μm observations.

The temperature structures characterizing their models were perturbed in a way which optimized the fit to our data between 40 and 100 μm.

As a baseline composition, we assumed a mixing ratio of 90% for H_2, close to those for Jupiter and Saturn. The remainder was assumed to be composed of He and CH_4. CH_4 influences the thermal spectrum in two ways. First, CH_4 collisions with H_2 change the H_2 collision-induced dipole absorption spectrum for that produced by H_2 or He collisions. Second, CH_4 condensation in the upper troposphere lowers the dry adiabatic lapse rate via latent heat (e.g. Eq. 3 of Wallace, 1980). The extent of this wet adiabat is controlled by the amount of CH_4 in the deep, uncondensed atmosphere. Three values for this mixing ratio were tested: 0.2%, 2% and 4%. The first is close to the Jovian value (Gautier et al. 1982), the second is an arbitrary "intermediate" value, and the last is a value recommended by Baines (1983). Values as high as 10% have been suggested for Uranus (Danielson, 1977), but these were judged by Orton et al. (1983) to be unlikely.

The approximate agreement between the shape of the model spectra of Uranus and Neptune and the data argues that the compositional assumptions implicit in the model are not unreasonable. The data in the 10- to 12-μm regions could be fitted better by thermal emission alone if the molar fraction of He were increased substantially (e.g. to 50%), but this is considered unlikely. Increasing the He mixing ratio substantially from the values used in the models tends to supress the H_2 rotational features at 16 and 27 μm, flatten the brightness temperature spectrum between 40 and 100 μm, and increase the rise in the brightness temperature toward longer wavelengths. The slow

variation of temperature with altitude, combined with the limited data set make it impossible to determine a trustworthy value for the He mixing ratio at this time, as in Gautier et al. (1981) for the Voyager IRIS spectra of Jupiter. On the other hand, it is clear that the immediate effect of replacing a substantial portion of the equilibrium H_2 by normal H_2 in the model is to increase the absorption in the 100- to 200- μm range relative to shorter wavelengths, making it much more difficult to fit both spectral regions simultaneously.

Some caution is warranted at this point. First, we are extending the models for H_2 collision-induced absorption well below the lowest temperature at which measurements have been made (cf. Dore et al. 1983), and the uncertainty involved in such an extrapolation is difficult to estimate. Other changes in the shape of the general continuum would take place under the influence of clouds in the atmosphere if the particle size were sufficiently large, as may occur in the atmosphere of Jupiter with NH_3 ice particles (Orton et al. 1982). Finally, changes in the He mixing ratio or the addition of normal-H_2 to equilibrium-H_2 in the model would change the effective specific heat of the atmosphere and influence the temperature lapse rate in the convective (adiabatic) part of the atmosphere for pressures greater than about 400 mbar. Such changes would influence the brightness temperature increase for wavelengths of about 200 μm and above and complicate the simple association we have presented between the brightness temperatures in the submillimeter and the mixing ratio of CH_4 in the deep atmosphere.

REFERENCES

Appleby, J.F. (1980). Atmospheric Structures of the Giant Planets from Radiative-Convective Equilibrium Models,Ph.D Thesis,State Univ. of New York, Stony Brook.

Aumann, H. H., C. M. Gillespie, and F. J. Low (1969). The internal powers and effective temperatures of Jupiter and Saturn. Astrophys. J. 157, L69-L72.

Baines, K. H. (1983). Interpretation of the 6818.9Å methane feature observed on Jupiter, Saturn and Uranus. Icarus. In press.

Beer, R. (1975). Detection of carbon monoxide in Jupiter. Astrophys. J. 200, L17-L19.

Bodenheimer, P., A. S. Grossman, W. M. DeCanpli, G. Marcy, and J. B. Pollack (1980). Calculations of the evolution of the giant planets. Icarus 41 293-308.

Cohen, E. R., L. Frommhold, and G. Birnbaum (1985). Analysis of the far infrared H_2-He spectrum. Astrophys. J. In press.

Courtin, R., D. Gautier, A. Marten and W. Maguire (1981). The acetylene and ethane abundances and the phosphine distribution in Saturn's atmosphere from the Voyager 1 - IRIS experiment. Bull. Amer. Astron. Soc. 13, 722.

Danielson, R. E. (1977). The structure of the atmosphere of Uranus. Icarus 30, 462-478.

Davies, M. E., V. K. Abalakin, C. A. Cross, R. L. Duncombe, H. Masursky, B. Morando, T. C. Owen, P. K. Seidelmann, A. T. Sinclair, G. A.Wilkins, and Y. C. Tjuflin (1980). Report of the IAU Working Group on cartographic coordinates and rotational elements of the planets and satellites. Celestial Mechanics 22 205-230.

Dore, P., L. Nencini, and G. Birnbaum (1983). Far infrared absorption in normal H_2 from 77K to 298K. J. Quant. Spectrosc. Radiat. Transfer 30 245-254. Elliot, J. L. (1979). Stellar occultation studies of the solar system. Ann Rev. Astron. Astrophys. 17, 445-475.

Elliot, J. L., E. Dunham, D. J. Mink, and J. Churms (1980). The radius and ellipticity of Uranus from its occultation of SAO 158687. Astrophys. J. 236, 1026-1030.

Elliot, J. L., R. G. French, J. A. Frogel, J. H. Elias, D. J. Mink, and W. Liller (1981). Orbits of nine Uranian rings. Astron. J. 86, 444-455.

Erickson, E. F., D. Goorvich, J. P. Simpson, and D. W. Strecker (1978). Far infrared brightness temperatures of Jupiter and Saturn. Icarus 35, 61-73.

Fazio, G. G., W. A. Traub, E. L. Wright, F. J. Low, and L. M. Trafton (1976). The effective temperature of Uranus. Astrophys. J. 209, 633-637.

Gautier, D., B. Conrath, M. Flasar, R. Hanel, V. Kunde, A. Chedin, and N. Scott (1981). The helium abundance of Jupiter from Voyager. J. Geophys. Res. 86, 8713-8720.

Gautier, D., B. Bezard, A. Marten, J.-P. Baluteau, A. Chedin, V. Kunde, and R. Hanel (1982). The C/H ratio in Jupiter from the Voyager infrared investigation. Astrophys. J. 257, 901-912.

Gautier, D., B.A. Conrath, R.A. Hanel, and J.S. Hornstein (1984).The helium abundance of Saturn from Voyager measurements. Astrophys. J. 282,807-815.

Graboske, H. C., Jr., J. B. Pollack, A. S. Grossman, and R. J. Olness (1975). The structure and evolution of Jupiter, the fluid contraction phase. Astrophys. J. 199, 265-281.

Grant, I. P., and G. E. Hunt (1969). Discrete space theory of radiative transfer. I. Fundamentals. Proc. Roy. Soc. London Ser. A 313, 183-197.

Hanel, R., B. Conrath, F. M. Flaser, V. Kunde, P. Lowman, W. Maguire, J. C. Pearl, J. A. Piraglia, R. Samuelson, D. Gautier, P. Gierasch, S. Kumar, and C. Ponnamperuma (1979). Infrared observations of the Jovian system from Voyager 1. Science 204, 972-976.

Hanel, R., B. Conrath, L. Herath, V. Kunde, and J. Pirraglia (1981). Albedo, internal heat, and energy balance of Jupiter: preliminary results of the Voyager infrared investigation. J. Geophys. Res. 86, 8705-8712.

Hanel, R., B. Conrath, F. M. Flaser, V. Kunde, W. Maguire, J. Pearl, J. Piraglia, R. Samuelson, D. Cruikshank, D. Gautier, P. Gierasch, L. Horn, and C. Ponnamperuma (1982). Infrared observations of the Saturnian system from Voyager 2. Science 215, 544-548.

Hanel, R. A., B. J. Conrath, V. G. Kunde, J. C. Pearl and J. A. Pirraglia (1983). Albedo, internal heat flux and energy balance of Saturn. Icarus 53, 262-285.

Holmes, A. W. (1981). Light scattering from ammonia in water crystals. Ph.D. Thesis, The University of Arizona, _____

Holmes, A. W., R. Paxman, H. P. Stahl, and M.G. Tomasko (1980). Light scattering by crystals of NH_3 and H_2O. Bull. Amer. Astron. Soc.

12, 705.

Hubbard W. B., and J. J. MacFarlane (1980). Structure and evolution of Uranus and Neptune. J. Geophys. Res. 85 225-234.

Husson, N., A. Goldman, and G. Orton (1981). Spectroscopic line parameters of NH_3 and PH_3 in the far infrared. J. Quant. Spectrosc. Radiat. Transfer 27, 505-515.

Husson, N., A. Chedin, N. A. Scott, I. Cohen-Hallaleh, and I. Berroir (1982). La banque de donnees "GEISA"; Mise a jour no. 3 (Juillet 1982). Note interne no. 116. Laboratoire de Meteorologie Dynamique, Ecole Polytechnique, Palaiseau, France.

Ingersoll, A. P., G. Munch, G. Neugebauer, and G. S. Orton (1976). Results of the infrared radiometer experiment on Pioneers 10 and 11. Jupiter ed. Gehrels, T. (University of Arizona Press).

Jaffe, D. T., R. H. Hildebrand, J. Keene, D. A. Harper, R. F. Loewenstein, and J. M. Moran (1984). Far-infrared selected star formation regions. Astrophys. J. 281, 225-236.

Kliore, A. J., I. R. Patel, G. F. Lindal, D. N. Sweetnam, H. B. Holtz, J. H. Waite Jr., and T. R. McDonough (1980). Structure of the ionosphere and atmosphere of Saturn from Pioneer 11 Saturn radio occultation. Jour. of Geophysical Research 85, 5857-5870.

Klein, M. J., M. A. Janssen, S. Gulkis, and E. T. Olsen (1978). Saturn's microwave spectrum: Implications for the atmosphere and the rings, in The Saturn System, NASA Conf. Publ. 2068, edited by D. M. Hunten and D. Morrison, pp. 195-216.

Kuhn, P. M., E. Magaziner, and L. P. Stearns (1976). Areal distribution

of water vapor burdon above the troposphere. Geophys. Res. Lett. 3 529.

Kunde, V., R. Hanel, W. Maguire, D. Gautier, J.-P. Baluteau, A. Marten, A. Chedin, N. Husson, and N. Scott (1982). The tropospheric gas composition of Jupiter's North Equatorial Belt (NH_3, PH_3, CH_3D, GeH_4, H_2O) and the Jovian D/H isotopic ratio. Astrophys. J. 263, 443-467.

Larson, H. P., U. Fink, and R. R. Treffers (1978). Evidence for CO in Jupiter's atmosphere from airborne spectroscopic observations at 5 microns. Astrophys. J. 219, 1084-1092.

Lindal, G. F., G. E. Wood, G. S. Levy, J. D. Anderson, D. N. Sweetnam, H. B. Hotz, B. J. Buckles, D. P. Holmes, P. E. Doms, V. R. Eshleman, G. L. Tyler, and T. A. Croft (1981). The atmosphere of Jupiter: an analysis of the Voyager occultation measurements. J. Geophys. Res. 86, 8721-8728.

Lockwood, G. W., B. L. Lutz, D. T. Thompson, and A. Warnock (1983). The albedo of Uranus. Astrophys. J. 266, 402-414.

Loewenstein, R. F., D. A. Harper, S. H. Moseley, C. M. Telesco, H. A. Thronson, R. H. Hildebrand, S. E. Whitcomb, R. Winston, and R. F. Stiening (1977a). Far infrared and submillimeter observations of the planets. Icarus 31, 315-324.

Loewenstein, R. F., D. A. Harper, and S. H. Moseley (1977b). The effective temperature of Neptune. Astrophys. J. 218, L145-L146.

Martonchik, J. V., G. S. Orton, and J. F. Appleby (1983). Optical properties of NH_3 ice from the far infrared through the near

ultraviolet. Appl. Optics. 23 541-551.

Mishima, O., D. D. Klug, and E. Whalley (1983). The far infrared spectrum of ice Ih in the range 8-25 cm^{-1}. Sound waves and difference bands, with application to Saturn's rings. J. Chem. Phys. 78 6399-6404.

Murphy, R. E., and L. M. Trafton (1974). Evidence for an internal heat source in Neptune. Astrophys. J. 193 253-255.

Neff, J. S., T. A. Ellis, J. Apt, and J. T. Bergstralh (1984). Bolometric geometric albedos of Titan, Uranus and Neptune. Bull. Amer. Astron. Soc. 16, 665.

Neugebauer, G., G. Munch, H. Kieffer, S. C. Chase Jr., and E. Miner, (1971). Mariner 1961 infrared radiometer results: temperature and thermal properties of the Martian surface. Astron. J. 76, 719-728.

Newburn, R. L., Jr., and S. Gulkis (1973). A survey of the outer planets Jupiter, Saturn, Uranus, Neptune, Pluto and their satellites. Space Science Rev. 14, 179-271.

Newburn, R. L., Jr., and S. Gulkis (1975). Planets and satellites of the outer solar system, asteroids, and comets. In Foundations of Space Biology and Medicine, Vol. I, NASA Spec. Publ. 274, edited by M. Calvin and O. G. Gazenko, pp. 197-268.

Orton, G. S. (1981). Modification to Scott's method for direct integration of gaseous transmission to improve speed and accuracy. J. Quant. Spectros. Radiat. Transfer 26, 463-466.

Orton, G. S., H. H. Aumann, J. V. Martonchik and J. F. Appleby (1982a). Airborne spectroscopy of Jupiter in the 100- to 300-cm^{-1} region:

Global properties of ammonia gas and ice haze. Icarus 52, 81-93.

Orton, G. S., J. F. Appleby and J. V. Martonchik (1982b). The effect of ammonia ice on the outgoing thermal radiance from the atmosphere of Jupiter. Icarus 52, 94-116.

Orton, G. S. (1983). Thermal infrared constraints on ammonia ice particles as candidates for clouds in the atmospheres of Saturn. Icarus 53, 293-300.

Orton, G. S., A. T. Tokunaga, and J. Caldwell (1983). Observational constraints on the atmospheres of Uranus and Neptune from new measurements near 10 m. Icarus 56 147-164.

Orton, G. S., M. J. Griffen, P. Ade, I. G. Nolt, J. V. Radostitz, E. I. Robson, W. K. Gear (1985). Submillimeter and millimeter observations of Uranus and Neptune. Submitted to Icarus.

Pirraglia, J. A., B. J. Conrath, M. D. Allison, and P. J. Gierasch (1981). Thermal structure and dynamics of Jupiter and Saturn. Nature 292, 677-679.

Pollack, J. B., and J. N. Cuzzi (1980). Scattering by nonspherical particles of size comparable to a wavelength: A new semi-empirical theory and its application to tropospheric aerosols. J. Atmos. Sci 37, 868-881.

Pollack, J. B., K. Rages, D. Wenkert, G. E. Danielson, J. Bergstralh, K. Baines, and J. S. Neff (1984). A determination of the bolometric albedo of Uranus and Neptune. Bull. Amer. Astron. Soc. 16, 657.

Scott, N. A. (1974). A direct method of computation of the transmission function of an inhomogeneous gaseous medium. J.

Quant. Spectros. Radiat. Transfer 14, 691-704.

Sill, G., U. Fink, and J. R. Ferraro (1980). Absorption coefficients of solid NH_3 from 50 to 7000 cm^{-1}. J. Opt. Soc. Amer. 70, 724-739.

Simpson, J. P., J. N. Cuzzi, E. F. Erickson, D. W. Strecker, and A. T. Tokunaga (1981). Mars: far infrared spectra and thermal-emission models. Icarus 48, 230-245.

Stevenson, D. J. (1980). Saturn's luminosity and magnetism. Science 208 746-748.

Stier, M. T., W. A. Traub, G. G. Fazio, E. L. Wright, F. J. Low (1978). Far-infrared observations of Uranus, Neptune, and Ceres. Astrophys. J. 226, 347-349.

Sweetnam, D. N. (1980). Viking radio occultation studies of the shape of Mars EOS Trans. Am. Geophys. Union 61, #46, P. 1020.

Tokunaga, A. T., H. L. Dinerstein, D. F. Lester, and D. M. Rank (1980). The phosphine abundance on Saturn derived from new 10-micrometer spectra. Icarus 42, 79-85.

Tokunaga, A. T., G. S. Orton, J. Caldwell (1983). New observational constraints on the temperature inversions of Uranus and Neptune. Icarus 53, 141-146.

Traub, W. A. and M.T. Stier, (1976). Theoretical atmospheric transmission in the mid- and infrared at four altitudes. Appl. Opt. 15, 364-377.

Tyler, G. L., V. R. Eshleman, J. D. Anderson, G. S. Levy, G. F. Lindal, G. E. Wood, and T. A. Croft (1982). Radio science with Voyager 2 at

Saturn: atmosphere and ionosphere and the masses of Mimas, Tethys, and Iapetus. Science 215, 553-557

Ulich, B. K. (1981). Millimeter-wavelength continuum calibration sources. Astron. J. 86, 1619-1626.

Wallace, L. (1980). The structure of the Uranus atmosphere. Icarus 43, 231-259.

Wenkert, D. D., G. E. Danielson, and J. B. Pollack (1984). Imaging of Uranus and Neptune from Voyager 1 and 2 and implications for their internal heat sources. B.A.A.S. 16, 659.

Whitcomb, S. E., R. H. Hildebrand, and Jocelyn Keene, R. F. Stiening, and D. A. Harper (1979). Submillimeter brightness temperature of Venus, Jupiter, Uranus and Neptune. Icarus 38, 75-80.

Whitcomb, S. E., R. H. Hildebrand, and J. Keene (1980). An f/35 submillimeter photometer for the NASA Infrared Telescope Facility. Pub. Astron. Soc. Pacific 92, 863-869.

Wright, E. L. (1976). Recalibration of the far-infrared brightness temperatures of the planets. Astrophys. J. 210, 250-253.

Wright, E. L., and S. Odenwald (1980). Brightness temperature of Mars. Bul. Amer. Astron. Soc. 12, 456.

FIGURE CAPTIONS

Figure 1: Transmission curves of the IRTF filters. The curves are labeled with the filter names used in the tables.

Figure 2: Transmission curves of the KAO filters. The curves are labeled with the filter names used in the tables.

Figure 3: The brightness temperature of Jupiter from KAO (circles) and IRTF (triangles). The dashed curve represents an initially assumed spectrum from which the solid curve was derived using an iterative procedure.

Numbers in parentheses indicate the number of data points occuring at that coordinate.

Errors are shown for the IRTF data, and are the statistical standard deviation of all measurements at that wavelength. No errors are shown for the KAO data, since statistical errors are small compared to systematic effects; instead, each measurement is plotted. The spread can be used to judge the extent of systematic errors.

Figure 4: The brightness temperature of Saturn. See Figure 3 caption.

Figure 5: The brightness temperature of Uranus. See Figure 3 caption.

Figure 6: The brightness temperature of Neptune. See Figure 3 caption.

Figure 7: Flux densities of Jupiter and Saturn. The curves correspond to the final derived (solid) curves in Figures 3 and 4. The individual data points are adjusted to a fixed planetary solid angle, and errors

shown are the standard deviation of the mean of the values of all observations at that wavelength.

Figure 8: Flux densities of Uranus and Neptune. The curves correspond to the final derived (solid) curves in Figures 5 and 6. See Figure 7 caption.

Figure 9: Spectra of Jupiter for models with no NH_3 cloud (upper curve), and for a cloud with a ratio of particle to gas scale heights H_p/H_g = 0.15 and particle sizes of 30 μm (middle curve) and 100 μm (lower curve). The spectra are computed with resolution element of 10 cm^{-1} through 100 μm (100 cm^{-1}), 5 cm^{-1} between 100 μm and 200 μm(50-100 cm^{-1}) and 2.5 cm^{-1} between 200μm and 1 mm (10-40 cm^{-1}). The spectrum at short wavelengths is taken from whole-disk Voyager IRIS average of Hanel et al. (1981). Tic marks in the upper graph denote the positions of strong lines or manifolds of NH_3 and PH_3.

Figure 10: Spectra of Jupiter for models with H_p/H_g = 0.50 and particle sizes of 10 μm (upper curve) and 100 μm (lower curve). Other symbols are shown as in Fig. 9.

Figure 11: Spectra of Jupiter for models with H_p/H_g = 0.05 and particle sizes of 10 μm (upper curve) and 100 μm (lower curve). Other symbols are shown as in Fig. 9.

Figure 12: Spectra of Saturn for models with various PH_3 mixing ratios. The curves represent spectra of models with the mixing ratio of PH_3 equal to 1.5 x 10^{-6} (upper curve), 3 x 10^{-6} (middle curve) and 1

x 10^{-5} (lower curve). The mixing ratio of NH_3 in the deep atmosphere equals 2 x 10^{-4}. Spectra are computed with resolution elements as given in Fig. 9. Tic marks in the upper graph have the same meaning as in Fig. 9.

Figure 13: Temperature structures of Uranus used in the models for a 90% mixing ratio of H_2. Each is a perturbation of the profile given by Tokunaga et al. (1982) which is nearly identical to the structures shown above the adiabatic region. The difference in temperature structures in the troposphere is the result of different wet adiabatic lapse rates associated with a variety of CH_4 mixing ratios in the deep atmosphere as shown.

Figure 14: Spectra of Uranus for 90% H_2 derived from the temperature structures shown in Fig. 13. Only the absorption of the collision-induced dipole of H_2 is considered in the models. Our data are shown by the filled circles. The 2% and 4% CH_4 spectra are indistinguishable at this scale near 50 m. From 10.3 to 19.6 m, the observations of Tokunaga et al. (1983) and Orton et al. (1983) are also shown as filled circles.

Figure 15: Temperature structures of Neptune used in the models for a 90% mixing ratio of H_2. Each is a perturbation of the profile given by Tokunaga et al. (1983), optimized to provide a best fit to our data between 40 and 100 m. The difference in tropospheric temperatures arises for the same reasons as for Uranus (Fig. 13).

Figure 16: Spectra of Neptune for 90% H_2 derived from the temperature structures shown in Figure 15. Only the absorption of the collision-induced H_2 dipole is considered in the models. The 2% and 4% CH_4 spectra are indistinguishable at this scale near 50 μm. From 10.3-to 19.6-μm, the observations of Tokunaga et al. (1983) and Orton et al. (1983) are also shown as filled circles.

TABLE I

ASSUMED PLANETARY RADII (1-bar)[a]

Planet	Equatorial Radius R_{eq} (km)	Ellipticity[b]	Pole Inclination[c] min - max
Mars	3397	0.006	111° - 115°
Jupiter	71495	0.065	87° - 89°
Saturn	60233	0.096	88° - 92°
Uranus	25563	0.024	19° - 27°
Neptune	24760	0.021	69° - 71°

[a] See Section III for references.

[b] $\epsilon = (R_{eq} - R_p)/R_{eq}$ where R_{eq} and R_p are the equatorial and polar radii.

[c] Range of angles between the planet pole and the line of sight during the observation.

TABLE II

JOURNAL OF OBSERVATIONS BROADBAND DATA

	(1)	(2)	(3)	(4)	(5)	(6)	(7)	(8)	(9)	(10)	(11)	(12)	(13)	(14)	(15)	(16)
Line	Planet		Date	Filter	r.o.s. H_2O		Zenith H_2O	λ[a]	Signal ratio	Semi-diameter[b]		Finite disk correction[c]		Brightness ratio[d]	Planet temperature	
	a	b	(UT)		w(a) (mm)	w(b) (mm)	(mm)	(μm)	S(a)/S(b)	Δ(a) (arc sec)	Δ(a)	D(a)	D(b)	B(a)/B(b)	T(b)[e] (K)	T(a)[f] (K)
1	Jup	Mars	1979 Nov 27	CH2	1.1	1.2	1.0	418	14.23 ± 0.18	17.78	3.66	1.185	1 006	0.710 ± 0.009	213	155.9 ± 1.8
2	Jup	Mars	1979 Nov 28	CH2	1.4	1.4	1.2	428	13.97 ± 0.17	17.83	3.69	1.186	1.006	0.705 ± 0.009	213	154.8 ± 1.8
3	Jup	Mars	1980 Feb 21	CH2	0.9	0.9	0.7	411	5.36 ± 0.38	21.64	6.86	1.306	1.020	0.690 ± 0.049	213.5	152.4 ± 9.7
	Jup			CH2												155.3 ± 1.3[g]
4	Jup	Mars	1980 May 23	MP2	4.5	4.4	2.7	952	19.34 ± 1.82	17.89	3.89	1.030	1.000	0.942 ± 0.089	199	187.9 ± 17 1
5	Jup	Mars	1980 May 25	MP2	5.9	5.9	4.5	992	17.82 ± 1.16	17.79	3.83	1.029	1.000	0.850 ± 0 056	199	170.2 ± 10 7
	Jup			MP2												175.1 ± 10.0[g]
6	Sat	Mars	1979 Nov 27	CH2	1.2	1.2	1.0	421	2.52 ± 0.03	8.12	3.66	1.032	1.006	0.525 ± 0.006	213	119.4 ± 1.2
7	Sat	Mars	1979 Nov 28	CH2	1.4	1.4	1.2	428	2.50 ± 0.04	8.13	3.69	1.031	1.009	0.526 ± 0.009	213	119.5 ± 1.8
8	Sat	Mars	1980 Feb 21	CH2	0.8	0.9	0.7	410	0.843 ± 0.065	9.27	6.86	1.042	1.020	0.471 ± 0.037	213.5	109.1 ± 7 3
	Sat			CH2												119.2 ± 1.2[g]
9	Sat	Mars	1980 May 23	MP2	3.4	4.4	2.7	936	3.33 ± 0.17	8.68	3.89	1.006	1.000	0.673 ± 0.035	199	136.4 ± 6.7
10	Sat	Mars	1980 May 25	MP2	5.4	5.9	4.5	986	3.35 ± 0.10	8.65	3.83	1.007	1.000	0.661 ± 0.019	199	133.9 ± 3.6
	Sat			MP2												134.5 ± 3.2[g]
11	Ur	Jup	1981 Mar 1	CH2	0.4	0.4	0.3	394	$(4.047 \pm 0.062)10^{-3}$	1.89	20.93	1.000	1.280	0.388 ± 0.006	155.3 ± 1.3	70.1 ± 1.3
12	Ur	Mars	1980 May 23	MP2	3.5	4.4	2.7	937	0.130 ± 0.020	1.98	3.89	1.000	1.000	0.502 ± 0.077	199	103.6 ± 14.8
13	Ur	Sat	1980 May 24	MP2	6.8	8.5	5.3	1020	0.038 ± 0.002	1.98	8.66	1.000	1 007	0.722 ± 0.038	134.5 ± 3.2	99.0 ± 5.3
14	Ur	Mars	1980 May 25	MP2	6.3	5.9	4.5	997	0.129 ± 0.011	1.98	3.83	1.000	1.000	0.483 ± 0.041	199	99.7 ± 7.9
15	Ur	Mars	1980 Jul 28	MP2	8.4	8.4	6.4	1012	0.209 ± 0.007	1.91	2.76	1.000	1.000	0.436 ± 0.014	203	92.4 ± 2.7
																94.5 ± 2.3[g]
16	Nept	Jup	1981 Mar 1	CH2	0.4	0.4	0.3	394	$(1.340 \pm 0.023)10^{-3}$	1.11	20.93	1.000	1.280	0.372 ± 0.006	155.3 ± 1.3	67.9 ± 1.2
17	Nept	Ur	1980 Jul 27	MP2	5.8	6.2	4.3	995	0.352 ± 0.050	1.15	1.91	1.000	1.000	0.971 ± 0 138	98.5 ± 2.3	92.0 ± 12.1
18	Nept	Mars	1980 Jul 28	MP2	9.0	8.4	6.4	1015	0.086 ± 0.008	1.14	2.76	1.000	1.000	0.504 ± 0.047	203	105.7 ± 9.2
19	Nept	Mars	1980 Jul 31	MP2	6.6	5.8	4.4	1000	0.112 ± 0.023	1.14	2.73	1.000	1.000	0.642 ± 0.133	203.5	133.1 ± 26.1
	Nept			MP2												103.0 ± 7.2[g]

a) Wavelength corresponding to effective frequency as given in equation (2) of text, for water vapor = $\frac{1}{2}$ [w(a) + w(b)]. See footnote f.
b) Based on assumed radii shown in Table IV.
c) From Figure 2, see section IIa.
d) $B(a)/B(b) = [S(a)/S(b)][\Phi(b)/\Phi(a)]^2[D(a)/D(b)]$
e) Mars temperatures based on Wright's model (1980) assuming no wavelength dependence for $\lambda \geq 350$ μm. Other temperatures from Table V.
f) For filters CH2 and MP2, T(a) is insensitive to λ (column 8) and hence to w(a) and w(b) (columns 5 and 6).
g) Average of values for same planet and filter.

TABLE III

JOURNAL OF OBSERVATIONS: NARROWER BAND DATA

Line	(1) Planet a	(2) Planet b	(3) Date (UT)	(4) Filters[a] x	(5) $\frac{S(ax)/S(ay)}{S(bx)/S(by)}$[b] s	(6) B(ay)/B(by)[c] t	(7) B(ax)/B(bx)[d] s·t	(8) T(bx)[e] (K)	(9) T(ax) (K)
1	Jup	Mars	1979 Nov 27	CH3	1.025 ± 0.040	0.710 ± 0.009	0.727 ± 0.030	213	160.0 ± 5.8
2	Jup	Mars	1979 Nov 28	CH3	1.088 ± 0.018	0.705 ± 0.009	0.767 ± 0.016	213	167.8 ± 3.1
3	Jup	Mars	1980 Feb 21	CH3	1.090 ± 0.040	0.690 ± 0.049	0.752 ± 0.060	213.5	164.9 ± 11.7
4	Jup	Mars	1980 Feb 22	CH3	1.036 ± 0.050	(0.707 ± 0.019)[f]	0.732 ± 0.040	213.5	161.0 ± 7.8
	Jup			CH3					165.5 ± 2.5[g]
5	Jup	Mars	1980 Feb 21	CH4	0.832 ± 0.004	0.690 ± 0.049	0.574 ± 0.041	213.5	128.9 ± 8.1
6	Jup	Mars	1980 Feb 22	CH4	0.870 ± 0.030	(0.707 ± 0.019)[f]	0.615 ± 0.027	213.5	137.1 ± 5.4
	Jup			CH4					134.6 ± 4.5[g]
7	Jup	Mars	1979 Nov 27	NO4	0.942 ± 0.019	0.710 ± 0.009	0.669 ± 0.016	213	146.9 ± 3.2
8	Jup	Mars	1979 Nov 28	NO4	0.980 ± 0.010	0.705 ± 0.009	0.691 ± 0.011	213	151.3 ± 2.2
	Jup			NO4					149.9 ± 2.6[g]
9	Jup	Mars	1979 Nov 27	CH5	1.090 ± 0.013	0.710 ± 0.009	0.774 ± 0.013	213	167.2 ± 2.6
10	Jup	Mars	1979 Nov 28	CH5	1.105 ± 0.030	0.705 ± 0.009	0.779 ± 0.023	213	168.2 ± 4.7
11	Jup	Mars	1980 Feb 21	CH5	1.053 ± 0.029	0.690 ± 0.049	0.727 ± 0.055	213.5	158.1 ± 11.1
12	Jup	Mars	1980 Feb 22	CH5	1.096 ± 0.040	(0.707 ± 0.019)[f]	0.775 ± 0.035	213.5	167.8 ± 7.1
	Jup			CH5					167.1 ± 2.1[g]
13	Sat	Mars	1979 Nov 27	CH3	0.924 ± 0.007	0.525 ± 0.006	0.485 ± 0.007	213	112.9 ± 1.4
14	Sat	Mars	1979 Nov 28	CH3	0.931 ± 0.003	0.526 ± 0.009	0.490 ± 0.009	213	113.9 ± 1.8
15	Sat	Mars	1980 Feb 21	CH3	0.897 ± 0.027	0.471 ± 0.037	0.422 ± 0.036	213.5	100.3 ± 7.1
16	Sat	Mars	1980 Feb 22	CH3	0.915 ± 0.30	(0.524 ± 0.015)[f]	0.479 ± 0.021	213.5	112.0 ± 4.1
	Sat			CH3					112.9 ± 1.1[g]
17	Sat	Mars	1980 Feb 21	CH4	0.970 ± 0.008	0.471 ± 0.037	0.457 ± 0.036	213.5	105.6 ± 7.1
18	Sat	Mars	1980 Feb 22	CH4	0.953 ± 0.020	(0.524 ± 0.015)[f]	0.499 ± 0.018	213.5	114.0 ± 3.6
	Sat			CH4					112.3 ± 3.2[g]
19	Sat	Mars	1979 Nov 27	NO4	1.020 ± 0.007	0.525 ± 0.006	0.536 ± 0.007	213	120.3 ± 1.4
20	Sat	Mars	1979 Nov 28	NO4	1.043 ± 0.005	0.526 ± 0.009	0.549 ± 0.010	213	122.9 ± 2.0
	Sat			NO4					122.2 ± 1.1[g]
21	Sat	Mars	1979 Nov 27	CH5	1.160 ± 0.017	0.525 ± 0.006	0.609 ± 0.011	213	133.8 ± 2.2
22	Sat	Mars	1979 Nov 28	CH5	1.317 ± 0.029	0.526 ± 0.009	0.693 ± 0.019	213	150.3 ± 3.9
23	Sat	Mars	1980 Feb 21	CH5	1.204 ± 0.016	0.471 ± 0.037	0.567 ± 0.045	213.5	125.5 ± 9.1
24	Sat	Mars	1980 Feb 22	CH5	1.174 ± 0.030	(0.524 ± 0.015)[f]	0.615 ± 0.024	213.5	135.3 ± 4.9
	Sat			CH5					137.1 ± 4.1[g]
25	Ur	Jup	1981 Mar 1	CH3	0.780 ± 0.034	0.338 ± 0.006	0.303 ± 0.014	165.5 ± 2.5	62.4 ± 2.3
26	Ur	Jup	1981 Mar 1	CH4	1.259 ± 0.083	0.388 ± 0.006	0.489 ± 0.033	134.6 ± 4.5	73.1 ± 4.5
27	Ur	Jup	1981 Mar 1	CH5	1.276 ± 0.101	0.388 ± 0.006	0.495 ± 0.040	167.1 ± 2.1	87.9 ± 6.4
28	Nep	Jup	1981 Mar 1	CH3	0.830 ± 0.042	0.372 ± 0.006	0.309 ± 0.016	165.5 ± 2.5	63.3 ± 2.5
29	Nep	Jup	1981 Mar 1	CH4	1.191 ± 0.178	0.372 ± 0.006	0.443 ± 0.067	134.6 ± 4.5	67.6 ± 8.4
30	Nep	Jup	1981 Mar 1	CH5	1.128 ± 0.151	0.372 ± 0.006	0.420 ± 0.057	167.1 ± 2.1	76.1 ± 9.0

[a] Filter y is CH2 in every case.

[b] S(ax)/S(ay) = ratio of signal from planet a with filter x (column 4) to signal from planet a with filter y (CH2), etc. The signal ratios have been corrected to 1 mm line-of-sight water vapor for filters CH2, CH3, CH4, NO4, and CH5, and to 5mm line-of-sight water vapor for MP2. The corresponding wavelengths are 414, 353, 450, 517, 664(1mm), and 938(5mm).

[c] B(ay) = brightness of planet a with filter y, etc. The values of the brightness ratios are taken from Table II column (14) using data from the same dates except as otherwise noted (footnote f)

[d] Column (5) times column (6).

[e] Assumed brightness temperature of planet b, filter x based on Wright's model (see Section III of text), where planet b is Mars, and on the results shown in Table V, where planet b is Jupiter.

[f] Average of earlier data on B(ay)/B(by) for same planets with error multiplied by 3. (No direct measurement of B(ay)/B(by) on February 22.)

[g] Average of values for same planet and filter.

TABLE IV

JOURNAL OF OBSERVATIONS AIRBORNE DATA

Line	(1) Planet a	(2) Planet b	(3) Date (UT)	(4) Filter (Aperture)	(5) w(a)	(6) w(b)	(7) Signal Ratio[b]	(8) Semi-diameter a(a) (arc sec)	(9) a(b)	(10) Finite Disk correction D(a)	(11) D(b)	(12) λ (μm)	(13) Flux Density (Jy)	(14) Planet Temp[c] T_b (K)
			1980											
1	Jup	Mars	May 2	G1-1(73)	6.3	6 2	4.31	19.03	4.54	1.097	1.005	38.7	1210000	134 9
2	Jup	Mars	May 2	G1-2(73)	6.3	6.1	6.69	19.03	4 54	1.097	1.005	55 1	1130000	138 5
3	Jup	Mars	May 2	G1-3(73)[f]	5.8	6.7	7.03	19.03	4.54	1 097	1.005	62 6	874000	129.0
4	Jup	Mars	May 2	G1-4(73)[f]	5.8	5.4	8 03	19.03	4.54	1.097	1.005	109 4	471000	131.5
5	Jup	Mars	May 2	G1-5(73)[f]	5 9	5.2	8 77	19.03	4 54	1.097	1.005	168 2	211000	118.8
6	Jup	Mars	May 2	S1-150(127)	6.3	6.3	8 92	19.03	4 54	1.031	1.002	135.4	330000	128.1
7	Jup	Mars	May 2	S1-200(127)	5.8	5 8	9.27	19.03	4 54	1 031	1 002	167 4	210000	117 9
8	Jup	Mars	May 2	S1-150L(127)	7.3	7.0	9 97	19.03	4 54	1.031	1.002	204 0	178000	132 7
9	Jup	Mars	May 2	S1-250(127)	6.5	5 2	10.05	19.03	4 54	1.031	1.002	221.8	156000	133 6
10	Jup	Mars	May 2	S1-250L(127)	6 9	6.6	10 41	19.03	4 54	1.031	1.002	328.6	83900	143 7
11	Sat	Mars	Jan 16	G1-1(49)	9 1	6 7	0.202	8.83	5.51	1.046	1.018	40 2	98500	99 4
12	Sat	Mars	Jan 16	G1-2(49)	9 1	6.9	0.442	8.83	5 51	1.046	1.018	56 1	113000	101.8
13	Sat	Mars	Jan 16	G1-3(49)	9.0	7.6	0.513	8.83	5.51	1.046	1.018	64 9	112000	103 9
14	Sat	Mars	Jan 16	G1-4(49)[g]	9.0	7.0	0 606	8.83	5.51	1.046	1.018	102.6	68000	99.3
15	Sat	Mars	Jan 16	G1-5(49)[g]	9.0	7 5	0 732	8.83	5 51	1 046	1.018	148 6	42500	99 9
16	Sat	Mars	Jan 16	S1-100(127)	9.0	6.8	0.668	8.83	5.51	1.007	1 003	99 4	67800	97.3
17	Sat	Mars	Jan 16	S1-150(127)	9.0	6 6	0.771	8.83	5 51	1 007	1.003	135 5	46600	97.6
18	Sat	Mars	Jan 16	S1-200(127)	9 3	6.9	0.838	8.83	5 51	1.007	1 003	168.1	33500	96 1
19	Sat	Mars	Jan 16	S1-150L(127)	9.0	6 9	0 903	8.83	5.51	1 007	1 003	205.2	25300	98 1
20	Sat	Mars	Jan 16	S1-250L(127)	9.0	6 3	1.033	8.83	5 51	1.007	1.003	331.6	12900	109 9
21	Sat	Mars	May 2	G1-1(73)	7.8	6.2	0.320	8 96	4 54	1.021	1 005	40.2	91700	96.8
22	Sat	Mars	May 2	G1-2(73)	7.6	6 1	0.728	8 96	4 54	1.021	1.005	56.2	112000	100 3
23	Sat	Mars	May 2	G1-3(73)[f]	7 5	6.7	0.870	8 96	4 54	1.021	1.005	65 9	113000	103 6
24	Sat	Mars	May 2	G1-4(73)[f]	8 4	5 4	1.20	8 96	4 54	1 021	1 005	110.8	66800	101 7
25	Sat	Mars	May 2	G1-5(73)[f]	8 1	5 2	1.38	8 96	4.54	1.021	1 005	169 3	35100	98 1
26	Sat	Mars	May 2	S1-150(127)	8 5	6.3	1.29	8.96	4 54	1.007	1.002	135 5	49900	100 0
27	Sat	Mars	May 2	S1-200(127)	8 7	5.8	1.32	8.96	4 54	1.007	1.002	168 1	33600	94 6
28	Sat	Mars	May 2	S1-150L(127)	9.3	7.0	1 44	8.96	4 54	1.007	1.002	205.2	25400	96 3
29	Sat	Mars	May 2	S1-250(127)	8 3	5.7	1 48	8 96	4 54	1.007	1.002	222 2	21600	94 1
30	Sat	Mars	May 2	S1-250L(127)	8.8	6.6	1.72	8 96	4.54	1.007	1.002	331.6	12900	106 9
31	Sat	Mars	May 13	G1-1(73)	9.3	8 1	0.361	8.81	4.17	1.020	1 005	40.2	86800	96 2
32	Sat	Mars	May 13	G1-2(73)	8 9	8.6	0.840	8.81	4 17	1.020	1 005	56.2	105000	99 4
33	Sat	Mars	May 13	G1-4(73)[f]	9 4	8 4	1 50	8.81	4 17	1.020	1.005	110 9	67200	104.0
34	Sat	Mars	May 13	G1-5(73)[f]	9.6	8.0	1 75	8.81	4 17	1.020	1.005	169 7	36600	103 4
35	Ur	Sat	May 7	G1-1(49)	11.0	11.7	0.00477 ± 20	1.98	8 90	1.002	1.046	42.8	536	59 9
36	Ur	Sat	May 7	G1-2(49)	10 4	11.7	0.00868 ± 0	1.98	8 90	1.002	1.046	57 7	924	59.6
37	Ur	Sat	May 7	G1-3(49)	11 4	11 7	0.0121 ± 2	1 98	8 90	1.002	1.046	74.0	1167	60.2
38	Ur	Sat	May 7	G1-4(49)[f]	11.0	12 1	0 0184 ± 2	1.98	8.90	1 002	1.046	115 1	1075	60 1
39	Ur	Sat	May 7	G1-5(49)[f]	11.0	12.1	0.0230 ± 3	1.98	8 90	1.002	1.046	166 7	973	60.9
40	Ur	Sat	May 7	S1-150(127)	11.1	12.0	0.0198 ± 9	1 98	8.90	1.000	1.007	136 9	915	59.3
41	Ur	Sat	May 7	S1-200(127)	10.7	12.3	0.0219 ± 9	1 98	8 90	1.000	1.007	172 5	723	59.2
42	Ur	Sat	May 7	S1-150L(127)	10.4	12.2	0.0244 ± 6	1.98	8 90	1.000	1.007	211.6	594	61.2
43	Ur	Sat	May 7	S1-250(127)	10.7	12.3	0.0260 ± 8	1 98	8.90	1.000	1.007	224 1	568	62 4
44	Ur	Sat	May 7	S1-250L(127)	11.4	12.2	0.0262 ± 18	1.98	8 90	1.000	1.007	329 7	324	63.5
			1982											
45	Ur[d]	Mars[e]	May 18	G2-1(49)	11.7	13.0	9.38×10^{-4}	1.97	5 93	1.000	1.020	42 8	583	60.6
46	Ur[d]	Mars[e]	May 18	G2-2(49)	11.8	13.0	3.59×10^{-3}	1.97	5.93	1.000	1.020	57 7	934	59 5
47	Ur[d]	Mars[e]	May 18	G2-4(49)[g]	11.8	12.0	$9 56 \times 10^{-3}$	1.97	5.93	1.000	1.020	115 2	990	58 4
48	Ur[d]	Mars[e]	May 18	G2-5(49)[g]	12.0	12.0	1.61×10^{-2}	1.97	5.93	1.000	1 020	166.8	803	61.7
49	Ur[d]	Mars[e]	May 18	G2-6(49)	11.8	14.0	1.04×10^{-2}	1 97	5 93	1.000	1.020	101.2	1062	58.6
50	Ur	Mars	May 18	G2-4(49)[h]	12.0	13.9	1.05×10^{-2}	1.97	5.93	1.000	1.020	115.8	878	55.7
51	Ur	Mars	May 18	G2-5(49)[h]	12.0	13.8	1.74×10^{-2}	1 97	5 93	1.000	1.020	168.8	733	59 2
52	Ur	Mars	May 18	G2-1(33)	11.8	12.0	1.02×10^{-3}	1.97	5 93	1.005	1.043	42.8	625	61 7
53	Ur	Mars	May 18	G2-2(33)	11.7	11.9	$3 72 \times 10^{-3}$	1 97	5 93	1.005	1.043	57.8	958	60 2
54	Ur[d]	Mars	Aug 29	G2-1(49)	14.0	15.0	$2 71 \times 10^{-3}$	1.86	3.20	1.000	1.006	42.8	494	60 4
55	Ur[d]	Mars	Aug 29	G2-2(49)	14.0	15.0	9.69×10^{-3}	1.86	3 20	1.000	1.006	57 7	740	58.3
56	Ur	Mars	Aug 29	G2-6(49)	14.0	15.0	2.62×10^{-2}	1.86	3.20	1.000	1.006	101.2	789	54.8
57	Ur	Mars	Sep 2	G2-1(49)	12.0	12.0	$2 45 \times 10^{-3}$	1.86	3 15	1.000	1.005	42.8	437	59 1
58	Ur	Mars	Sep 2	G2-2(49)	12.0	12.0	9.85×10^{-3}	1.86	3 15	1.000	1.005	57.8	742	58 3
59	Ur	Mars	Sep 2	G2-4(49)[g]	12 0	12.0	$2 44 \times 10^{-2}$	1.86	3 15	1.000	1.005	115.2	719	53 7
60	Ur	Mars	Sep 2	G2-5(49)[g]	12.0	12.0	4.02×10^{-2}	1.86	3 15	1.000	1.005	166.8	588	55 7
61	Nep[d]	Ur	May 16	G2-1(49)	7	7	0 408 ± 34	1 15	1.97	1.000	1.000	41.8	184	60.8
62	Nep[d]	Ur	May 16	G2-2(49)	7	7	0.369 ± 8	1 15	1 97	1.000	1.000	58 1	347	61.0
63	Nep[d]	Ur[e]	May 16	G2-4(49)[h]	7	7	0 378 ± 8	1 15	1 97	1 000	1.000	113 3	361	59.8
64	Nep[d]	Ur[e]	May 16	G2-5(49)[h]	7	7	0 355 ± 13	1 15	1 97	1.000	1 000	164 7	267	60 4
65	Nep[d]	Ur[e]	May 16	G2-6(49)	7	7	0 402 ± 15	1 15	1 97	1.000	1.000	101 1	399	60.8
66	Nep[d]	Ur	May 16	G2-1(33)	7	7	0.375 ± 22	1 15	1 97	1 000	1.000	41.8	168	59.8
67	Nep	Ur	May 16	G2-2(33)	7	7	0 366 ± 9	1 15	1 97	1.000	1.000	58.2	345	60 9
68	Nep	Ur	May 16	G2-6(33)	7	7	0 384 ± 17	1 15	1.9[illegible]	1.000	1.000	99 7	382	59 7
69	Nep	Ur[e]	Aug 29	G2-1(49)	11.0	14 0	0 466	1 14	1 86	1.000	1.000	41.8	181	60 7
70	Nep	Ur[e]	Aug 29	G2-2(49)	11.0	14.0	0 420	1 14	1.86	1.000	1 000	58.0	338	60 9
71	Nep	Ur	Aug 29	G2-4.49,[g]	11.0	14 0	0 406	1.14	1.86	1 000	1 000	113 6	328	57 9
72	Nep	Ur[e]	Aug 29	G2-5(49)[g]	11.0	14.0	0 414	1 14	1.86	1.000	1.000	165 3	265	60 9
73	Nep	Ur	Aug 29	G2-6(49)	11.0	14 0	0 386	1 14	1.86	1.000	1.000	101.0	324	56.6
			1983											
74	Ur	Jup	Jun 4	H1-1(73)	13.0	12 0	.00177	1 96	21.89	1 000	1 127	105 9	1017	58 2
75	Ur	Jup	Jun 4	H1-3(73)	13.0	12.0	.00205 ± 6	1 96	21.89	1 000	1 127	137.2	798	56 3
76	Ur	Jup	Jun 4	H1-6(73)	12.0	11.0	.00270 ± 2	1 96	21.89	1.000	1 127	19 1	618	58 7
77	Ur	Jup	Jun 4	H1-7(73)	12.0	11.0	.00272 ± 2	1 96	21.89	1.000	1 12[illegible]	198.2	590	58 [illegible]

[a] Line of sight water vapor based on a boresight radiometer for lines 1 to 44 and on a zenith radiometer and secant z for lines 45 to 73 On May 16 (lines 61 to 68) the zenith radiometer failed before the planet observations A typical zenith value was used to estimate the boresight value

[b] The errors in the least significant digits are shown in cases where repeated measurements permitted statistical error analysis

[c] We estimate the statistical errors (not including the errors in the Mars calibration) at 1 5K for Jupiter, Saturn and Uranus, and 3 5K for Neptune

[d] Two observations of planet a averaged

[e] Two observations of planet b averaged.

[f] The short-wavelength blocking filter was Teflon

[g] For these measurements filters 4 and 5 were used without any Teflon or CaF_2 for short-wavelength blocking The data have been corrected taking into account a small measured leak at ~ 20 μ

[h] The short-wavelength blocking filter was CaF_2

BRIGHTNESS TEMPERATURES[a]

(Summary of Data from Tables II, III, and IV)

Line	Jupiter		Saturn		Uranus		Neptune	
	λ (μm)	Temp (K)	λ (μm)	Temp (K)	λ (μm)	Temp (K)	λ (μm)	Temp (K)
1	38.7	134.0	40.2	97.5 ± 1.7[b]	42.8	60.3 ± 0.7[c]	41.8	60.6 ± 0.5[c]
2	55.1	138.5	56.2	100.5 ± 1.2[b]	57.7	59.2 ± 0.7[c]	58.1	60.9 ± 0.1[c]
3	62.6	129.0	65.4	103.7 ± 0.2[b]	74.0	60.2	100.8	58.9 ± 2.1[c]
4	109.4	131.5	99.4	97.3	102.8	57.2 ± 2.1[b]	113.4	58.9 ± 1.3[b]
5	135.4	128.1	102.6	99.3	115.3	57.0 ± 2.8[b]	165.0	60.7 ± 0.4[b]
6	168.0	118.4 ± 0.6[b]	110.8	102.9 ± 1.6[b]	137.0	57.8 ± 2.1[b]		
7	204.0	132.7	135.5	98.8 ± 1.7[b]	167.3	59.4 ± 2.7[b]		
8	221.8	133.6	148.6	99.9	172.5	59.2		
9					191.1	58.7		
10					198.2	58.7		
11	328.6	143.7	168.6	97.2 ± 3.3[b]	211.6	61.2		
12			205.2	97.2 ± 1.3[b]	224.1	62.4		
13			222.2	94.1	329.7	63.5		
14			331.6	108.4 ± 2.1[b]				
15	353	165.5 ± 2.5	353	112.9 ± 1.1	353	62.4 ± 2.3	353	63.3 ± 2.5
16	414	155.3 ± 1.3	414	119.2 ± 1.2	414	70.1 ± 1.3	414	67.9 ± 1.2
17	450	135 ± 5	450	112.3 ± 3.2	450	73 ± 5	450	68 ± 8
18	517	149.9 ± 2.6	517	122.2 ± 1.1				
19	664	167.1 ± 2.1	664	137 ± 4	664	88 ± 6	664	76 ± 9
20	968	175 ± 10	968	134.5 ± 3.2	968	94.5 ± 2.3	968	103 ± 7

[a]None of the errors shown in this table includes the uncertainty in the Mars calibration. Errors for IRTF data (lines 13-18) are computed as specified in Appendix D. Errors shown for KAO data (lines 1-12) are standard deviations of two or more measurements from Table IV where the effective wavelengths fall within a range of 2 μm. (See footnotes b and c concerning weighting.) The mean of the 19 errors for KAO data is 1.5 K (see discussion in text).

[b]Average of data for bandpass and low pass filters with values of λ_{eff} within 2 μm. Bandpass measurements are given twice the weight of low pass measurements.

[c]Average of data for 33" and 49" apertures (λ_{eff} within 2 μm). To allow for possible guiding errors the 33" measurements are given half the weight of 49" measurements.

TABLE VI

Effective temperature T_e and ratios, E/A, of
emitted to absorbed energy with assumed Bond Albedos

Planet	T_e[a]	E/A[a]	Bond Albedo	reference
Jupiter	126.8 ± 4.4K	1.8 ± 0.3	0.343 ± 0.032	Hanel et al., 1981
Saturn	93.4 ± 3.3K	1.7 ± 0.3	0.342 ± 0.030	Hanel et al., 1983
Uranus	58.3 ± 2.0K	1.2 ± 0.2	0.393 ± 0.037	Lockwood et al., 1983
Neptune	60.3 ± 2.0K	2.8 ± 0.4	0.29	see text

[a] Errors reflect an assumed 15% absolute calibration error in flux.

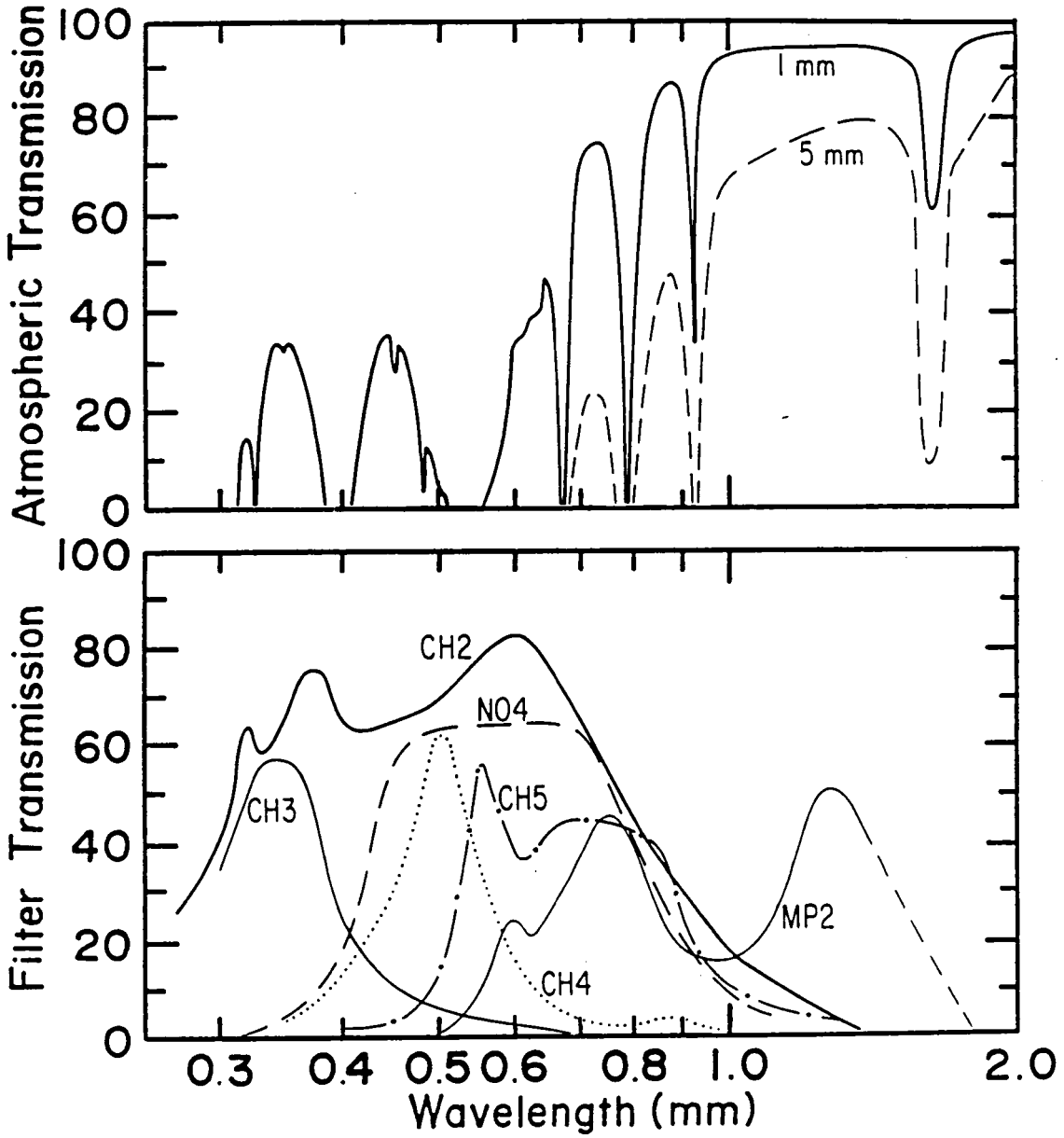
Atmospheric Transmission
100
80
60
40
20
0
1 mm
5 mm
Filter Transmission
100
80
60
40
20
0
CH2
NO4
CH3
CH5
MP2
CH4
0.3
0.4
0.5
0.6
0.8
1.0
2.0
Wavelength (mm)

Fig. 1

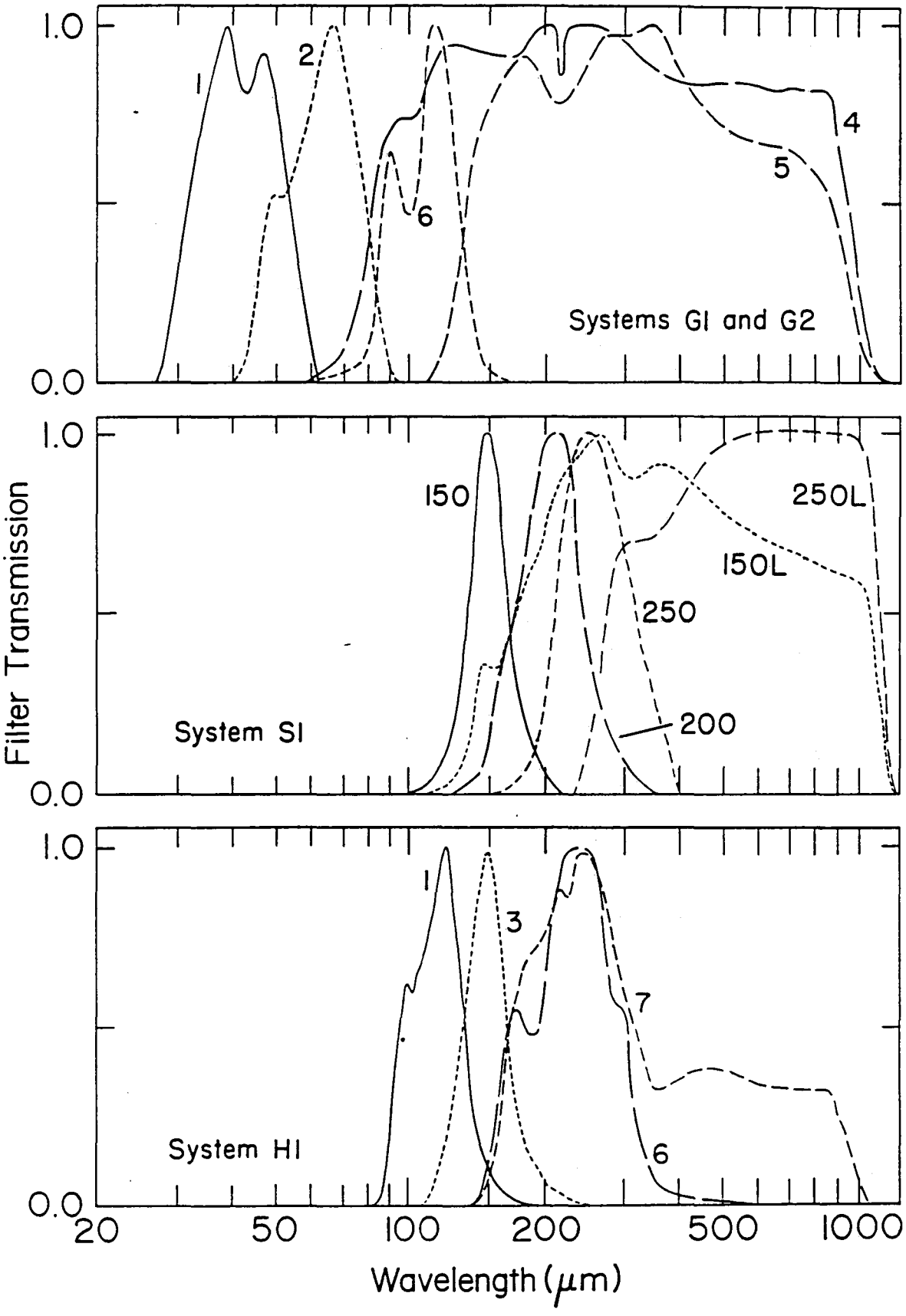
1.0
0.0
1
2
6
4
5
Systems GI and G2
1.0
0.0
150
250L
150L
250
200
System SI
Filter Transmission
1.0
0.0
1
3
7
6
System HI
20
50
100
200
500
1000
Wavelength (μm)

Fig. 2

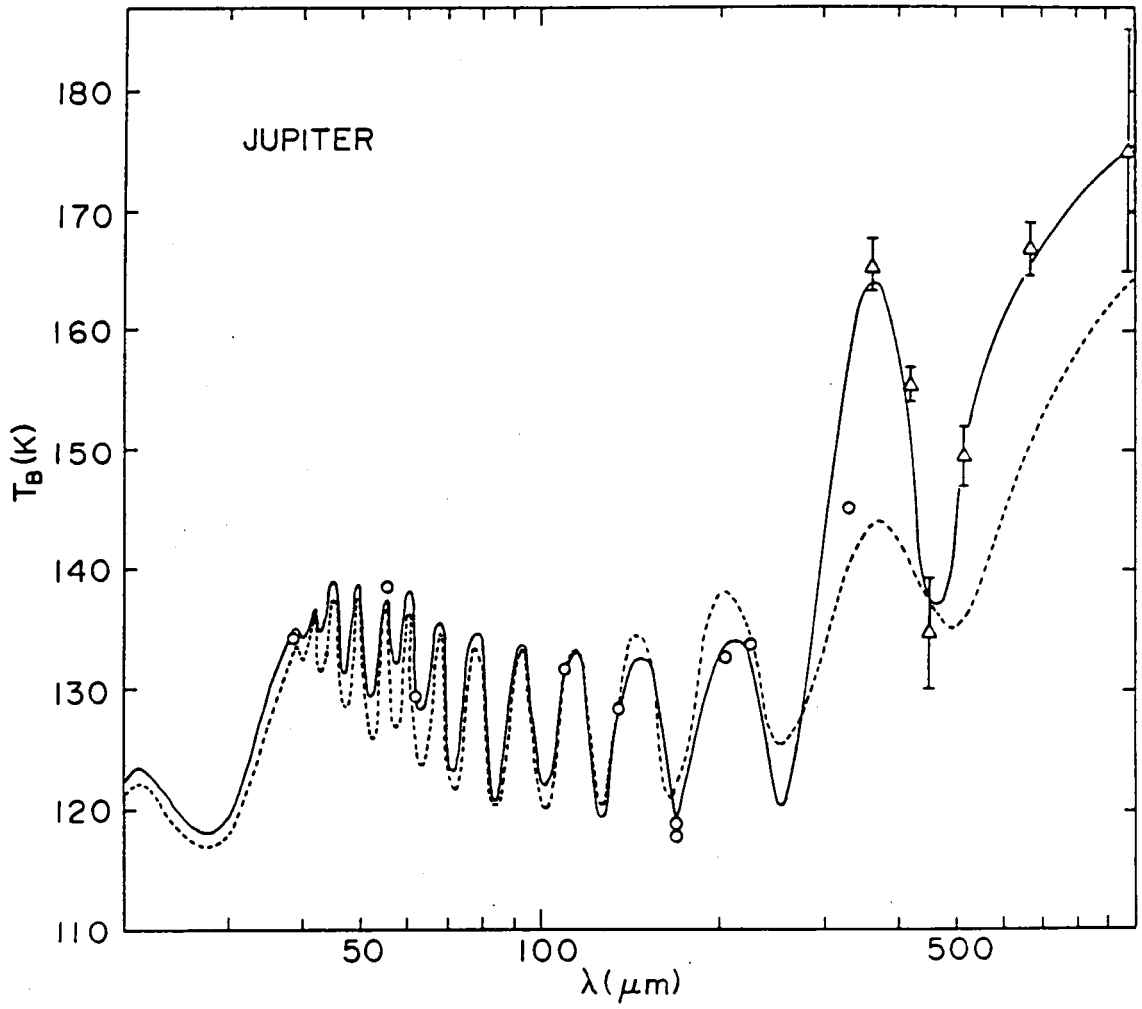

Fig. 3

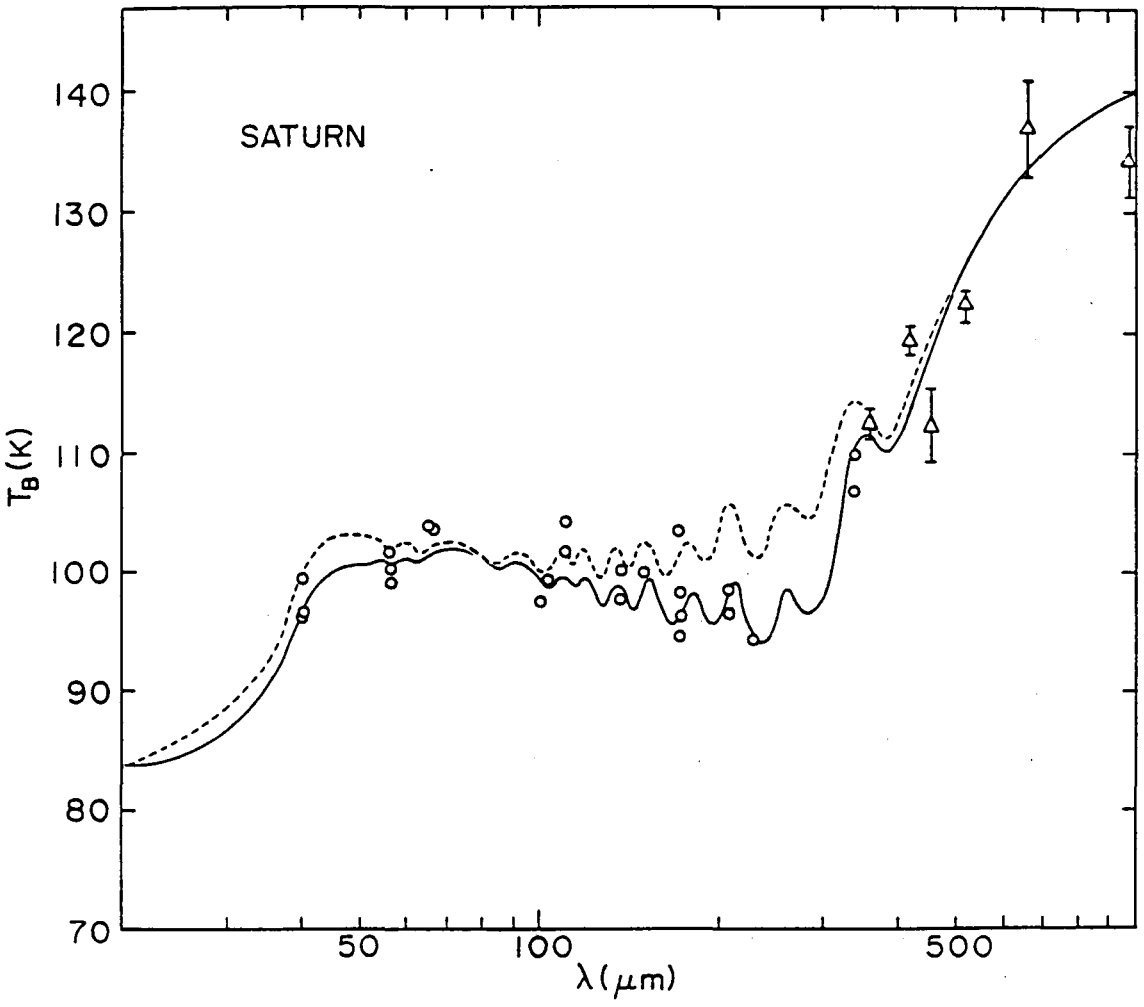

Fig. 4

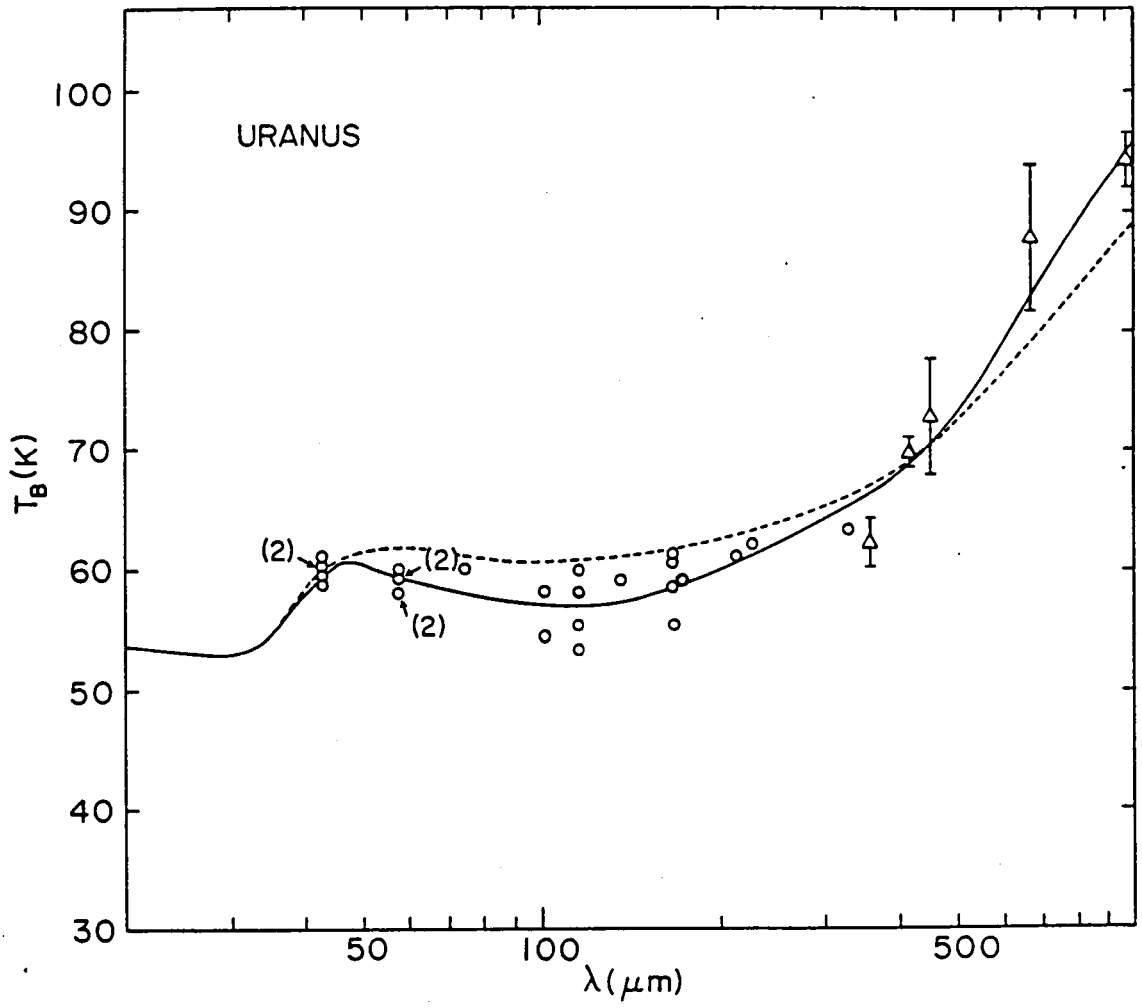

Fig. 5

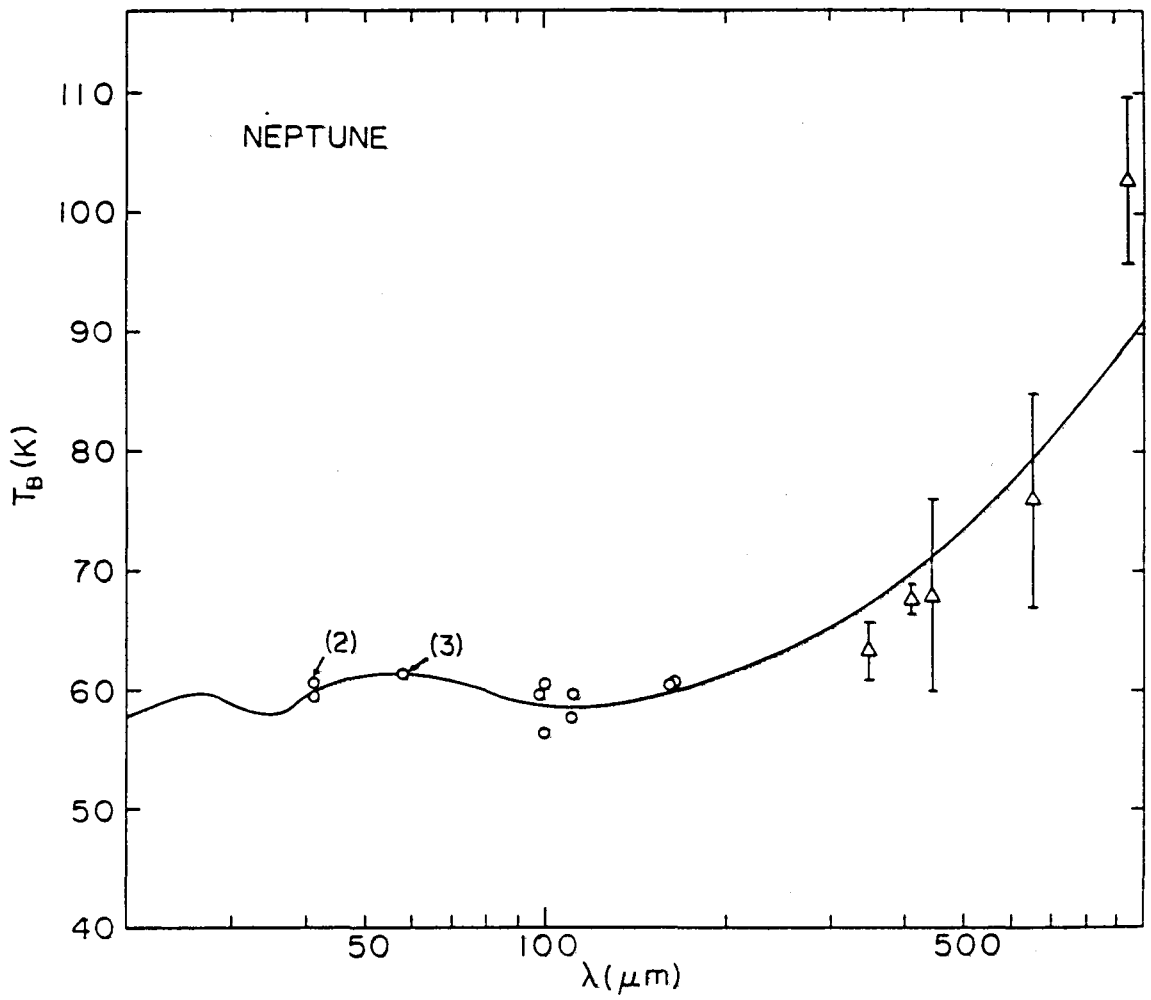

Fig. 6

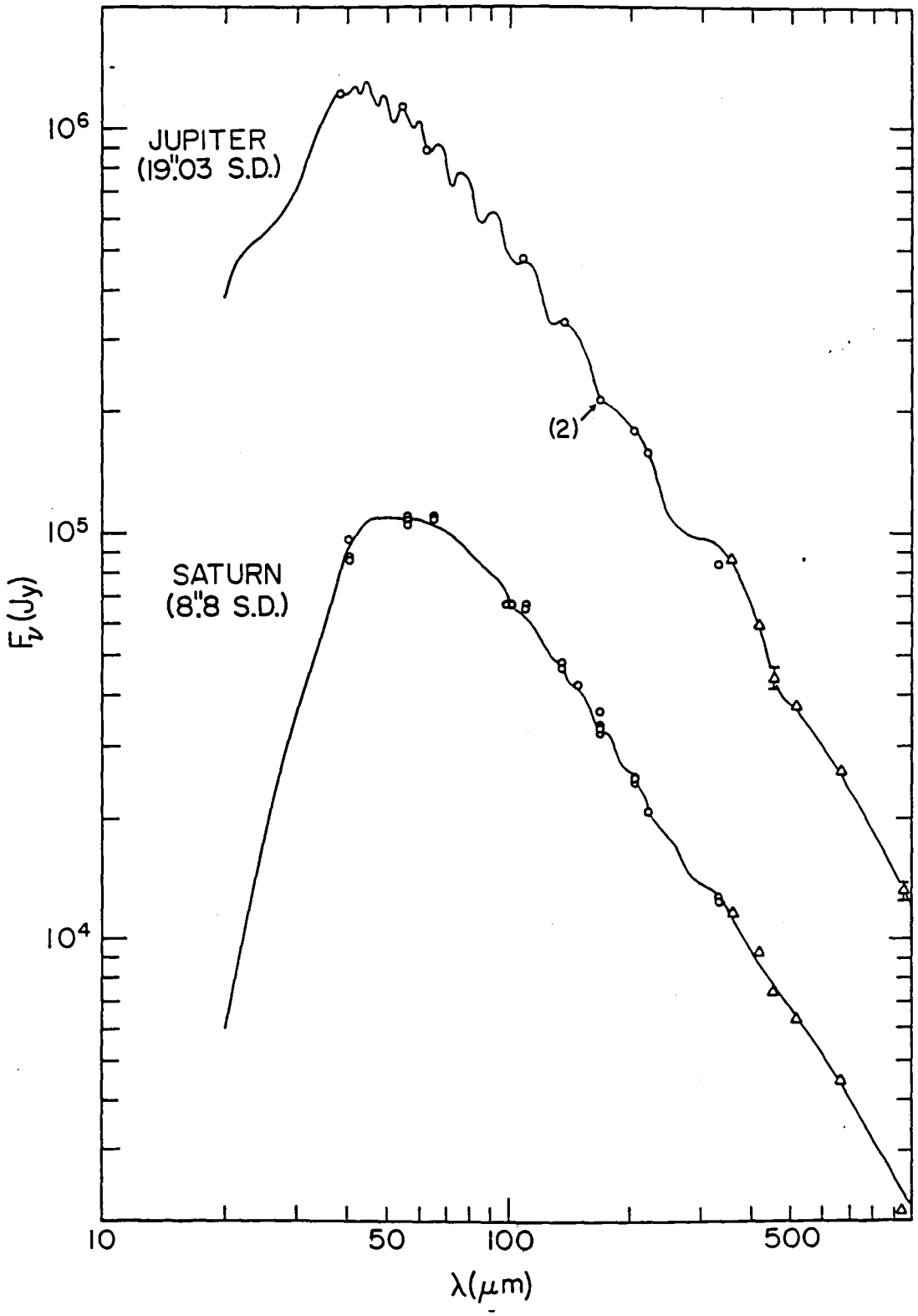
JUPITER
(19".03 S.D.)
(2)
SATURN
(8".8 S.D.)
10^6
10^5
10^4
F_ν (Jy)
10
50
100
500
λ(μm)

Fig. 7

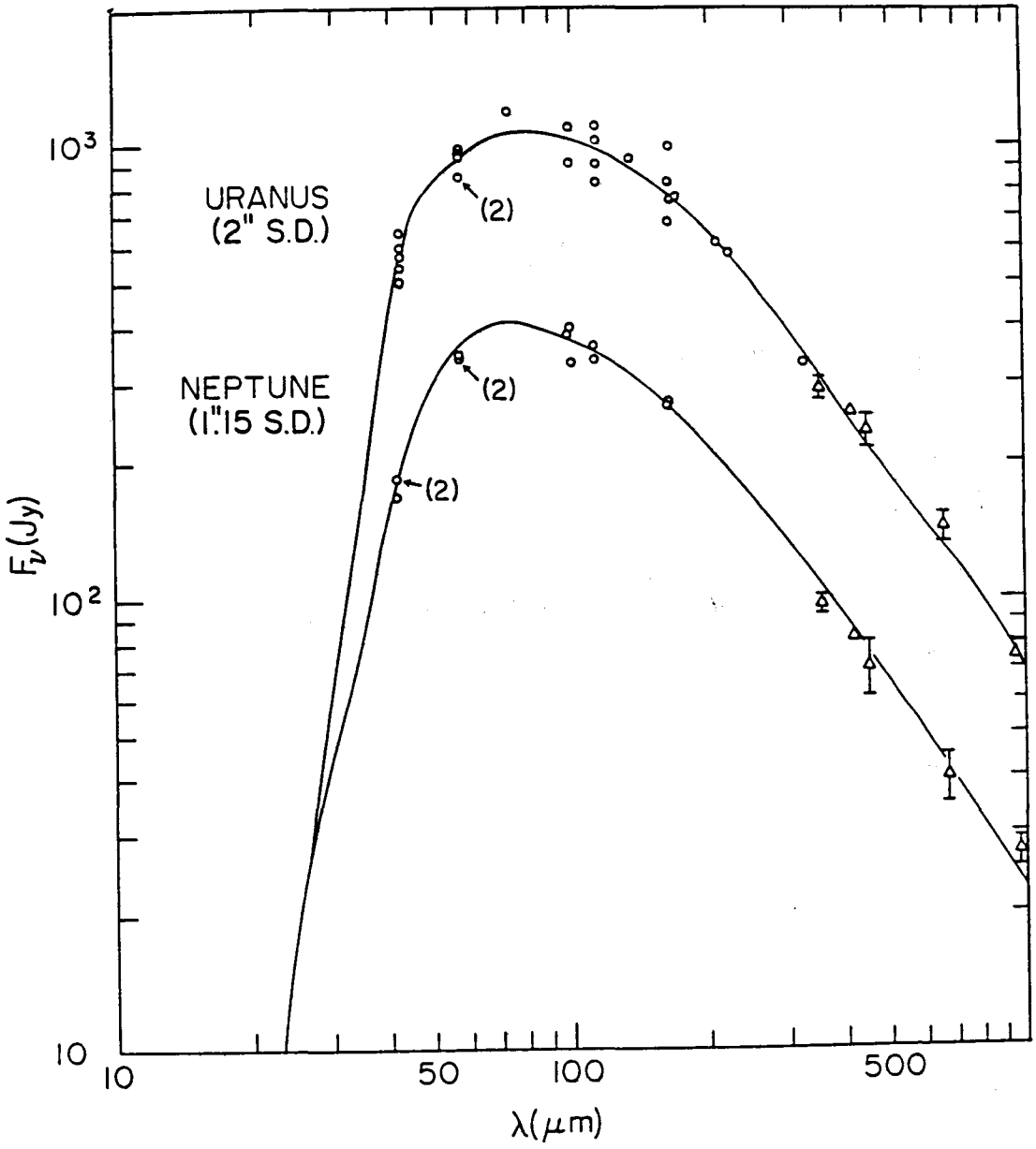
URANUS
(2" S.D.)
NEPTUNE
(1".15 S.D.)
(2)
(2)
(2)
10^3
10^2
10
F_ν(Jy)
10
50
100
500
λ(μm)

Fig. 8

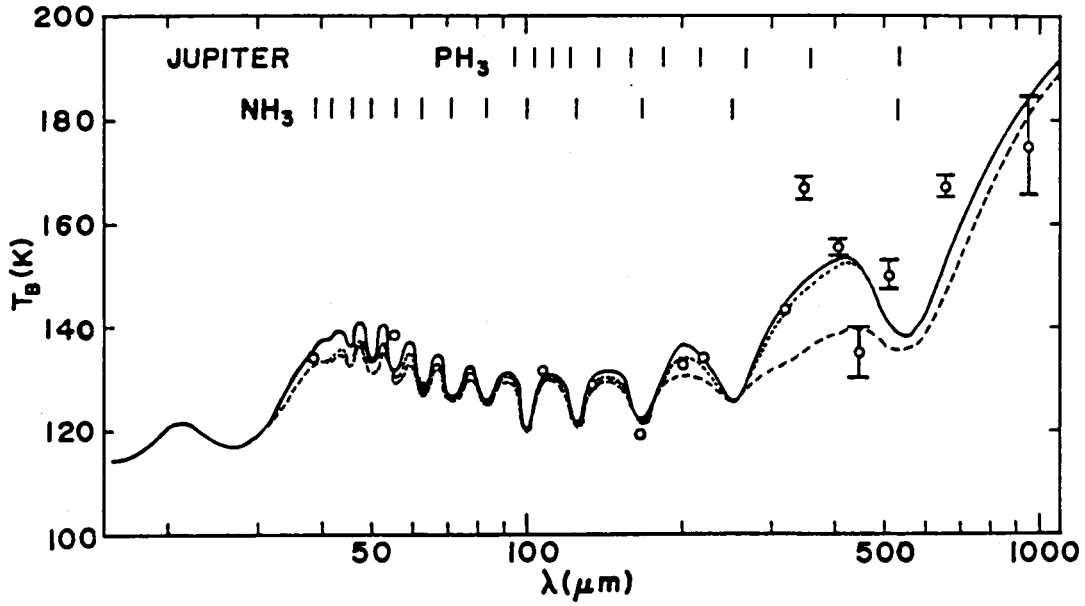

Fig. 9

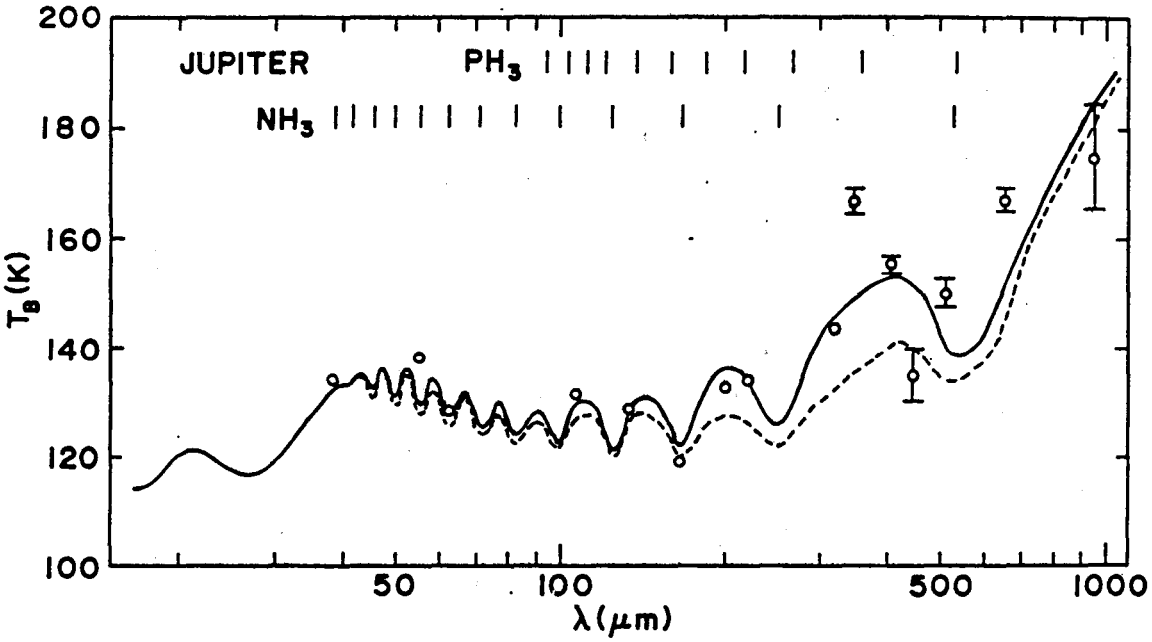

Fig. 10

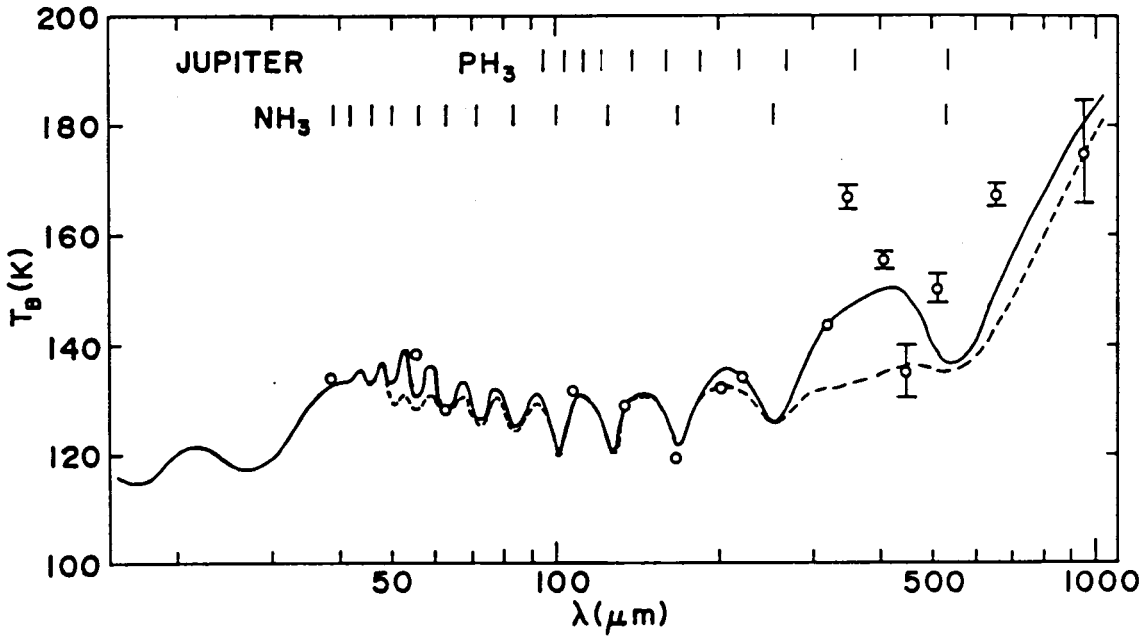

Fig. 11

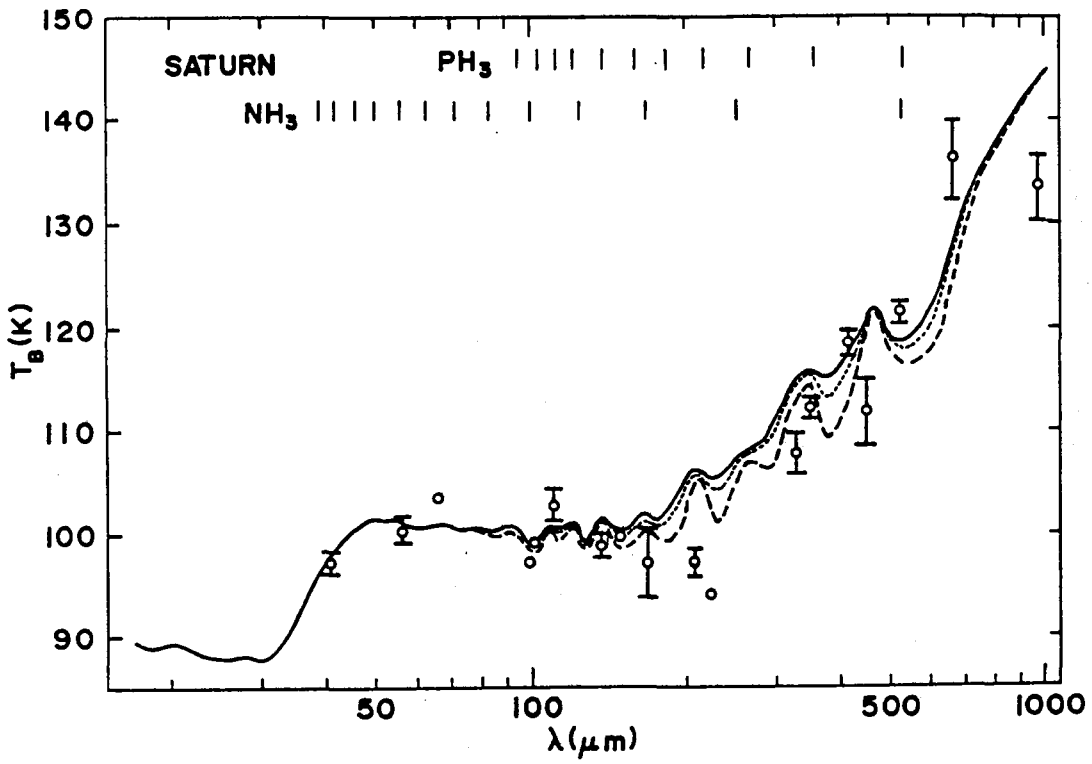
SATURN
PH3
NH3
150
140
130
120
110
100
90
TB(K)
50
100
500
1000
λ(μm)

Fig. 12

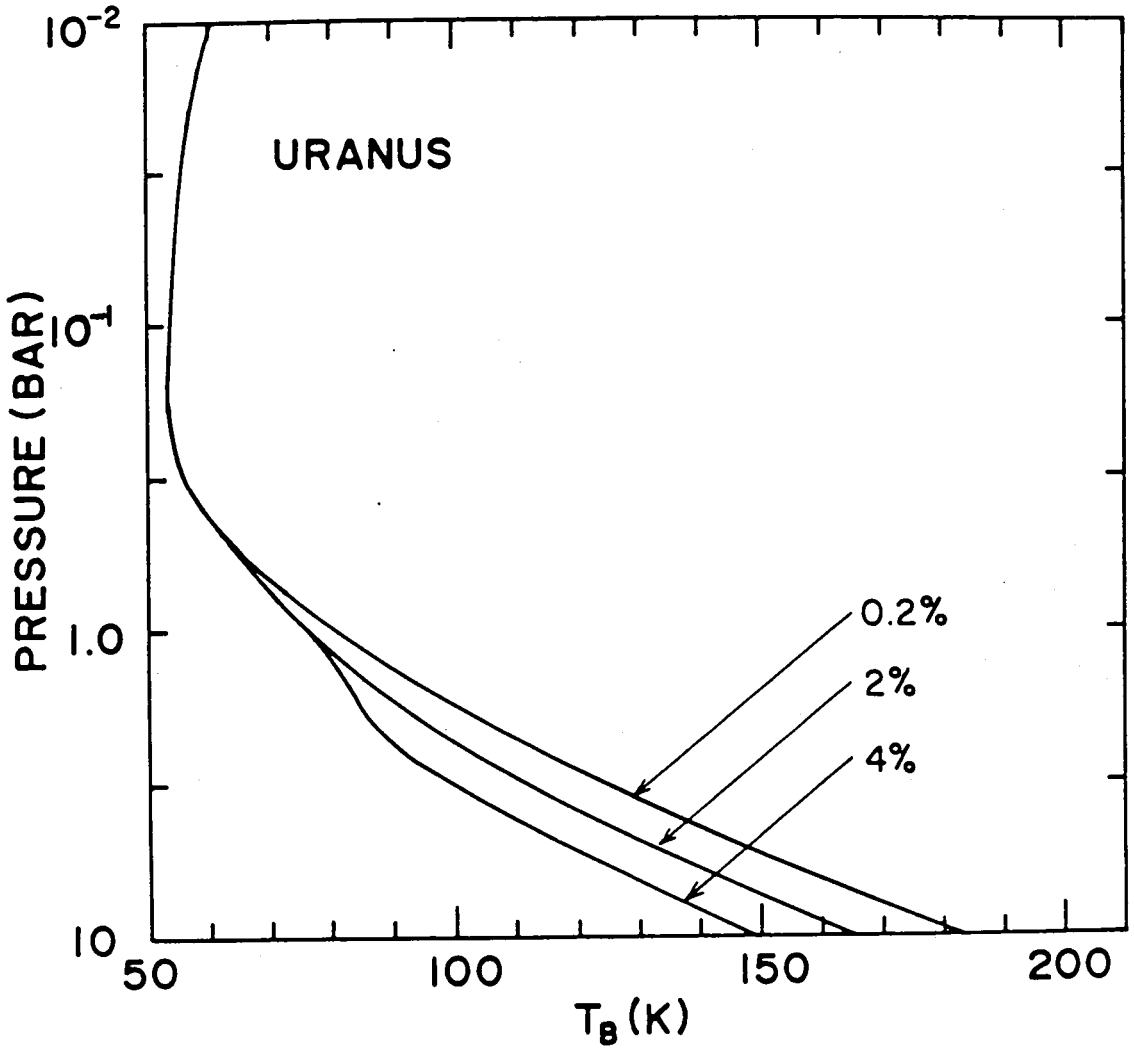

Fig. 13

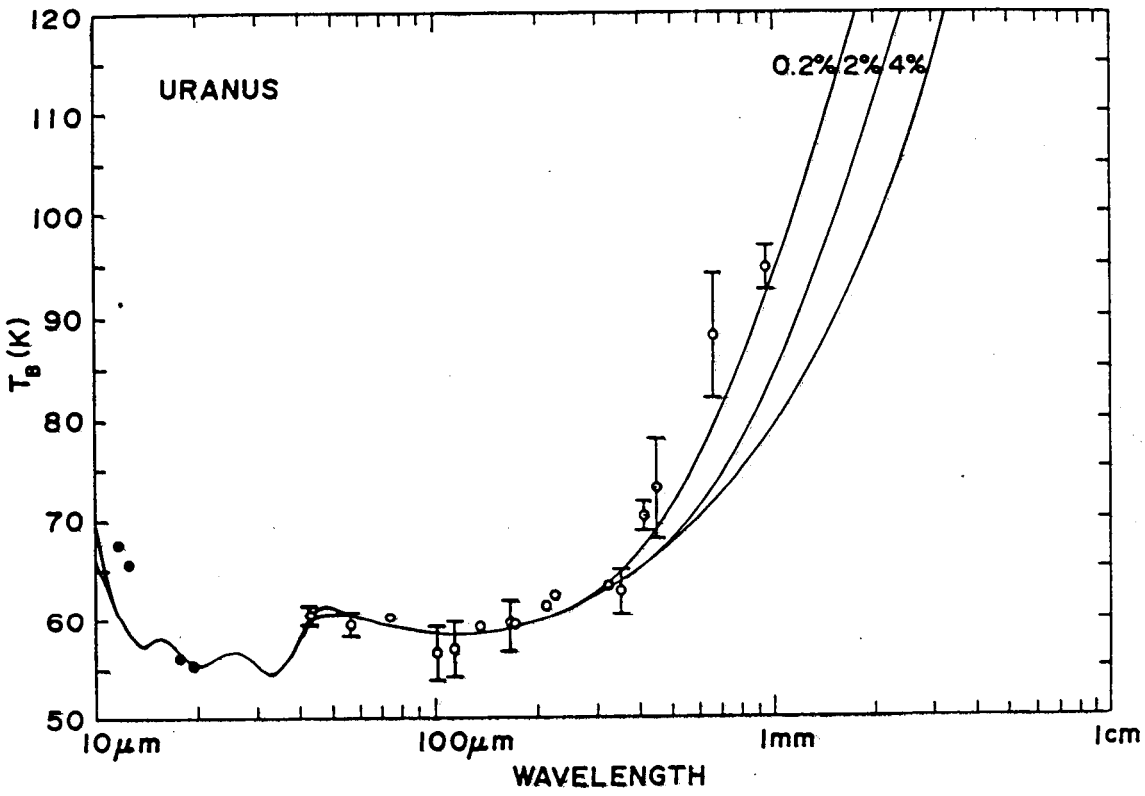
URANUS
0.2%
2%
4%
120
110
100
90
80
70
60
50
T_B (K)
10μm
100μm
1mm
1cm
WAVELENGTH

Fig. 14

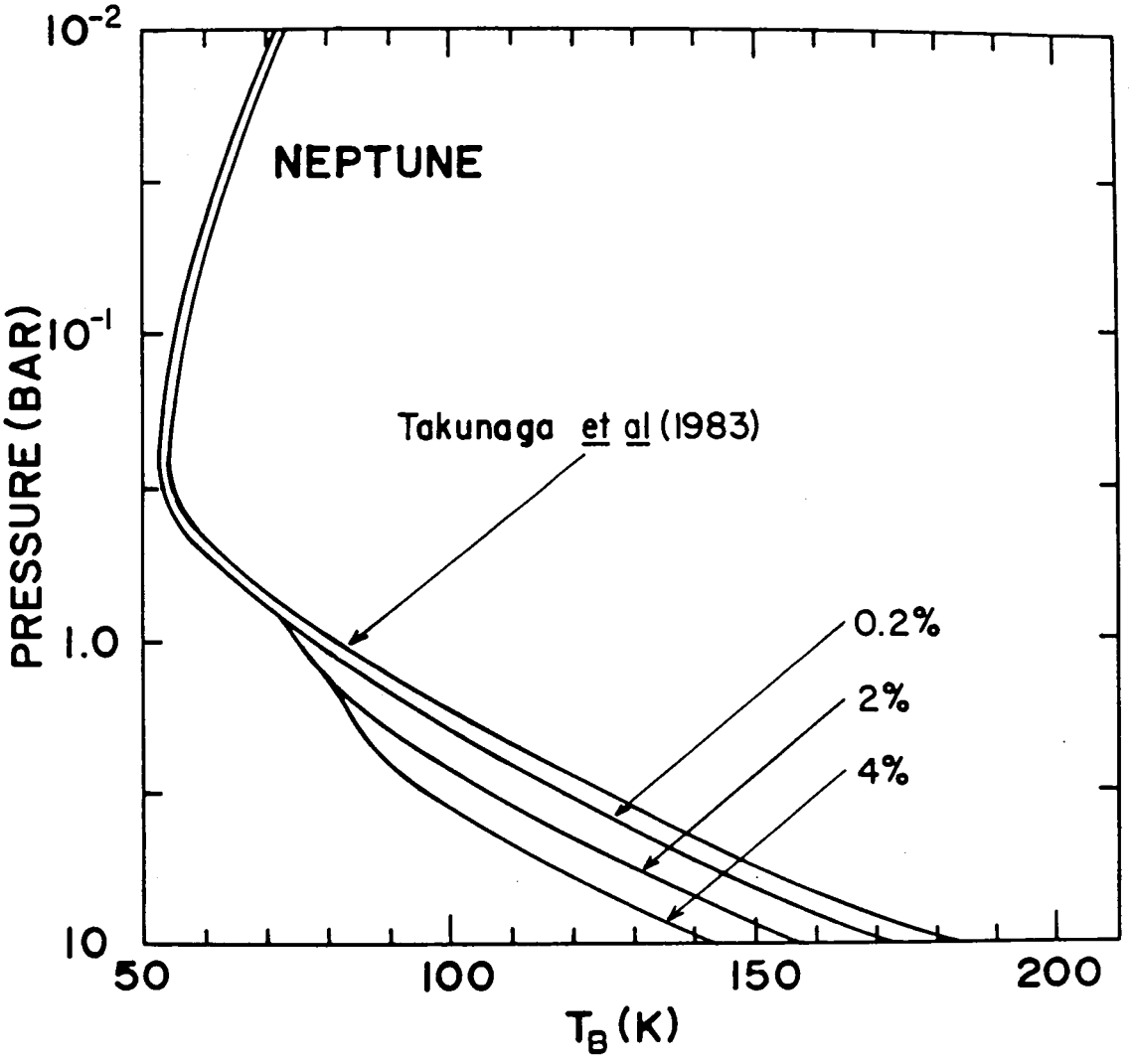
NEPTUNE
Takunaga et al (1983)
0.2%
2%
4%
PRESSURE (BAR)
10^{-2}
10^{-1}
1.0
10
50
100
150
200
T_B (K)

Fig. 15

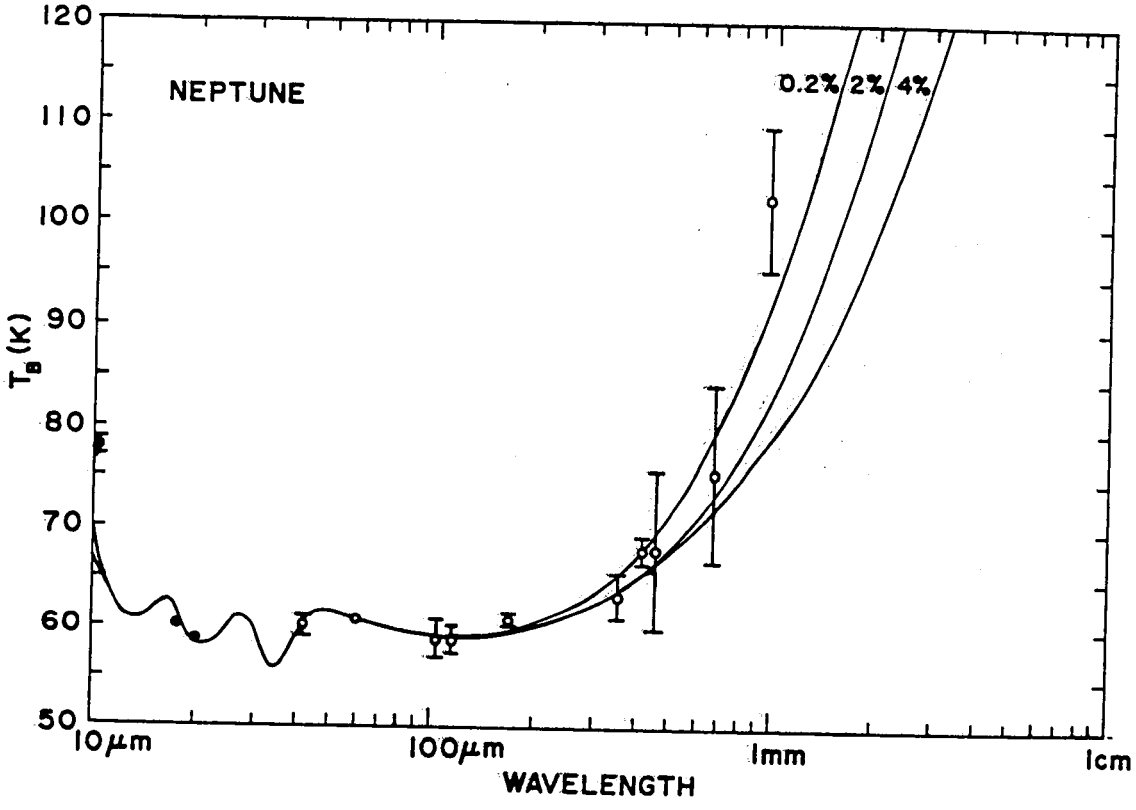
NEPTUNE
0.2%
2%
4%
120
110
100
90
80
70
60
50
T_B (K)
10μm
100μm
1mm
1cm
WAVELENGTH

Fig. 16

TABLE I

ASSUMED PLANETARY RADII (1-bar)[a]

Planet	Equatorial Radius R_{eq} (km)	Ellipticity[b]	Pole Inclination[c] min - max
Mars	3397	0.006	111° - 115°
Jupiter	71495	0.065	87° - 89°
Saturn	60233	0.096	88° - 92°
Uranus	25563	0.024	19° - 27°
Neptune	24760	0.021	69° - 71°

[a] See Section III for references.

[b] $\epsilon = (R_{eq} - R_p)/R_{eq}$ where R_{eq} and R_p are the equatorial and polar radii.

[c] Range of angles between the planet pole and the line of sight during the observation.

TABLE II

JOURNAL OF OBSERVATIONS: BROADBAND DATA

Line	Planet a	Planet b	Date (UT)	Filter	l.o.s. H_2O w(a) (mm)	l.o.s. H_2O w(b) (mm)	Zenith H_2O (mm)	λ[a] (μm)	Signal ratio S(a)/S(b)	Semi-diameter[b] Δ(a) (arc sec)	Semi-diameter[b] Δ(a) (arc sec)	Finite disk correction[c] D(a)	Finite disk correction[c] D(b)	Brightness ratio[d] B(a)/B(b)	Planet temperature T(b)[e] (K)	Planet temperature T(a)[f] (K)
1	Jup	Mars	1979 Nov 27	CH2	1.1	1.2	1.0	418	14.23 ± 0.18	17.78	3.66	1.185	1.006	0.710 ± 0.009	213	155.9 ± 1.8
2	Jup	Mars	1979 Nov 28	CH2	1.4	1.4	1.2	428	13.97 ± 0.17	17.83	3.69	1.186	1.006	0.705 ± 0.009	213	154.8 ± 1.8
3	Jup	Mars	1980 Feb 21	CH2	0.9	0.9	0.7	411	5.36 ± 0.38	21.64	6.86	1.306	1.020	0.690 ± 0.049	213.5	152.4 ± 9.7
	Jup			CH2												155.3 ± 1.3[g]
4	Jup	Mars	1980 May 23	MP2	4.5	4.4	2.7	952	19.34 ± 1.82	17.89	3.89	1.030	1.000	0.942 ± 0.089	199	187.9 ± 17.1
5	Jup	Mars	1980 May 25	MP2	5.9	5.9	4.5	992	17.82 ± 1.16	17.79	3.83	1.029	1.000	0.850 ± 0.056	199	170.2 ± 10.7
	Jup			MP2												175.1 ± 10.0[g]
6	Sat	Mars	1979 Nov 27	CH2	1.2	1.2	1.0	421	2.52 ± 0.03	8.12	3.66	1.032	1.006	0.525 ± 0.006	213	119.4 ± 1.2
7	Sat	Mars	1979 Nov 28	CH2	1.4	1.4	1.2	428	2.50 ± 0.04	8.13	3.69	1.031	1.009	0.526 ± 0.009	213	119.5 ± 1.8
8	Sat	Mars	1980 Feb 21	CH2	0.8	0.9	0.7	410	0.843 ± 0.065	9.27	6.86	1.042	1.020	0.471 ± 0.037	213.5	109.1 ± 7.3
	Sat			CH2												119.2 ± 1.2[g]
9	Sat	Mars	1980 May 23	MP2	3.4	4.4	2.7	936	3.33 ± 0.17	8.68	3.89	1.006	1.000	0.673 ± 0.035	199	136.4 ± 6.7
10	Sat	Mars	1980 May 25	MP2	5.4	5.9	4.5	986	3.35 ± 0.10	8.65	3.83	1.007	1.000	0.661 ± 0.019	199	133.9 ± 3.6
	Sat			MP2												134.5 ± 3.2[g]
11	Ur	Jup	1981 Mar 1	CH2	0.4	0.4	0.3	394	$(4.047 \pm 0.062)10^{-3}$	1.89	20.93	1.000	1.280	0.388 ± 0.006	155.3 ± 1.3	70.1 ± 1.3
12	Ur	Mars	1980 May 23	MP2	3.5	4.4	2.7	937	0.130 ± 0.020	1.98	3.89	1.000	1.000	0.502 ± 0.077	199	103.6 ± 14.8
13	Ur	Sat	1980 May 24	MP2	6.8	8.5	5.3	1020	0.038 ± 0.002	1.98	8.66	1.000	1.007	0.722 ± 0.038	134.5 ± 3.2	99.0 ± 5.3
14	Ur	Mars	1980 May 25	MP2	6.3	5.9	4.5	997	0.129 ± 0.011	1.98	3.83	1.000	1.000	0.483 ± 0.041	199	99.7 ± 7.9
15	Ur	Mars	1980 Jul 28	MP2	8.4	8.4	6.4	1012	0.209 ± 0.007	1.91	2.76	1.000	1.000	0.436 ± 0.014	203	92.4 ± 2.7
																94.5 ± 2.3[g]
16	Nept	Jup	1981 Mar 1	CH2	0.4	0.4	0.3	394	$(1.340 \pm 0.023)10^{-3}$	1.11	20.93	1.000	1.280	0.372 ± 0.006	155.3 ± 1.3	67.9 ± 1.2
17	Nept	Ur	1980 Jul 27	MP2	5.8	6.2	4.3	995	0.352 ± 0.050	1.15	1.91	1.000	1.000	0.971 ± 0.138	98.5 ± 2.3	92.0 ± 12.1
18	Nept	Mars	1980 Jul 28	MP2	9.0	8.4	6.4	1015	0.086 ± 0.008	1.14	2.76	1.000	1.000	0.504 ± 0.047	203	105.7 ± 9.2
19	Nept	Mars	1980 Jul 31	MP2	6.6	5.8	4.4	1000	0.112 ± 0.023	1.14	2.73	1.000	1.000	0.642 ± 0.133	203.5	133.1 ± 26.1
	Nept			MP2												103.0 ± 7.2[g]

a) Wavelength corresponding to effective frequency as given in equation (2) of text, for water vapor = $\frac{1}{2}$ [w(a) + w(b)]. See footnote f.
b) Based on assumed radii shown in Table IV.
c) From Figure 2; see section IIa.
d) $B(a)/B(b) = [S(a)/S(b)][\Phi(b)/\Phi(a)]^2[D(a)/D(b)]$.
e) Mars temperatures based on Wright's model (1980) assuming no wavelength dependence for $\lambda \geq 350$ μm. Other temperatures from Table V.
f) For filters CH2 and MP2, T(a) is insensitive to λ (column 8) and hence to w(a) and w(b) (columns 5 and 6).
g) Average of values for same planet and filter.

TABLE III

JOURNAL OF OBSERVATIONS: NARROWER BAND DATA

	(1)	(2)	(3)	(4)	(5)	(6)	(7)	(8)	(9)
Line	Planet a	Planet b	Date (UT)	Filters[a] x	$\frac{S(ax)/S(ay)}{S(bx)/S(by)}$[b] s	B(ay)/B(by)[c] t	B(ax)/B(bx)[d] s·t	T(bx)[e] (K)	T(ax) (K)
1	Jup	Mars	1979 Nov 27	CH3	1.025 ± 0.040	0.710 ± 0.009	0.727 ± 0.030	213	160.0 ± 5.8
2	Jup	Mars	1979 Nov 28	CH3	1.088 ± 0.018	0.705 ± 0.009	0.767 ± 0.016	213	167.8 ± 3.1
3	Jup	Mars	1980 Feb 21	CH3	1.090 ± 0.040	0.690 ± 0.049	0.752 ± 0.060	213.5	164.9 ± 11.7
4	Jup	Mars	1980 Feb 22	CH3	1.036 ± 0.050	(0.707 ± 0.019)[f]	0.732 ± 0.040	213.5	161.0 ± 7.8
	Jup			CH3					165.5 ± 2.5[g]
5	Jup	Mars	1980 Feb 21	CH4	0.832 ± 0.004	0.690 ± 0.049	0.574 ± 0.041	213.5	128.9 ± 8.1
6	Jup	Mars	1980 Feb 22	CH4	0.870 ± 0.030	(0.707 ± 0.019)[f]	0.615 ± 0.027	213.5	137.1 ± 5.4
	Jup			CH4					134.6 ± 4.5[g]
7	Jup	Mars	1979 Nov 27	NO4	0.942 ± 0.019	0.710 ± 0.009	0.669 ± 0.016	213	146.9 ± 3.2
8	Jup	Mars	1979 Nov 28	NO4	0.980 ± 0.010	0.705 ± 0.009	0.691 ± 0.011	213	151.3 ± 2.2
	Jup			NO4					149.9 ± 2.6[g]
9	Jup	Mars	1979 Nov 27	CH5	1.090 ± 0.013	0.710 ± 0.009	0.774 ± 0.013	213	167.2 ± 2.6
10	Jup	Mars	1979 Nov 28	CH5	1.105 ± 0.030	0.705 ± 0.009	0.779 ± 0.023	213	168.2 ± 4.7
11	Jup	Mars	1980 Feb 21	CH5	1.053 ± 0.029	0.690 ± 0.049	0.727 ± 0.055	213.5	158.1 ± 11.1
12	Jup	Mars	1980 Feb 22	CH5	1.096 ± 0.040	(0.707 ± 0.019)[f]	0.775 ± 0.035	213.5	167.8 ± 7.1
	Jup			CH5					167.1 ± 2.1[g]
13	Sat	Mars	1979 Nov 27	CH3	0.924 ± 0.007	0.525 ± 0.006	0.485 ± 0.007	213	112.9 ± 1.4
14	Sat	Mars	1979 Nov 28	CH3	0.931 ± 0.003	0.526 ± 0.009	0.490 ± 0.009	213	113.9 ± 1.8
15	Sat	Mars	1980 Feb 21	CH3	0.897 ± 0.027	0.471 ± 0.037	0.422 ± 0.036	213.5	100.3 ± 7.1
16	Sat	Mars	1980 Feb 22	CH3	0.915 ± 0.30	(0.524 ± 0.015)[f]	0.479 ± 0.021	213.5	112.0 ± 4.1
	Sat			CH3					112.9 ± 1.1[g]
17	Sat	Mars	1980 Feb 21	CH4	0.970 ± 0.008	0.471 ± 0.037	0.457 ± 0.036	213.5	105.6 ± 7.1
18	Sat	Mars	1980 Feb 22	CH4	0.953 ± 0.020	(0.524 ± 0.015)[f]	0.499 ± 0.018	213.5	114.0 ± 3.6
	Sat			CH4					112.3 ± 3.2[g]
19	Sat	Mars	1979 Nov 27	NO4	1.020 ± 0.007	0.525 ± 0.006	0.536 ± 0.007	213	120.3 ± 1.4
20	Sat	Mars	1979 Nov 28	NO4	1.043 ± 0.005	0.526 ± 0.009	0.549 ± 0.010	213	122.9 ± 2.0
	Sat			NO4					122.2 ± 1.1[g]
21	Sat	Mars	1979 Nov 27	CH5	1.160 ± 0.017	0.525 ± 0.006	0.609 ± 0.011	213	133.8 ± 2.2
22	Sat	Mars	1979 Nov 28	CH5	1.317 ± 0.029	0.526 ± 0.009	0.693 ± 0.019	213	150.3 ± 3.9
23	Sat	Mars	1980 Feb 21	CH5	1.204 ± 0.016	0.471 ± 0.037	0.567 ± 0.045	213.5	125.5 ± 9.1
24	Sat	Mars	1980 Feb 22	CH5	1.174 ± 0.030	(0.524 ± 0.015)[f]	0.615 ± 0.024	213.5	135.3 ± 4.9
	Sat			CH5					137.1 ± 4.1[g]
25	Ur	Jup	1981 Mar 1	CH3	0.780 ± 0.034	0.338 ± 0.006	0.303 ± 0.014	165.5 ± 2.5	62.4 ± 2.3
26	Ur	Jup	1981 Mar 1	CH4	1.259 ± 0.083	0.388 ± 0.006	0.489 ± 0.033	134.6 ± 4.5	73.1 ± 4.5
27	Ur	Jup	1981 Mar 1	CH5	1.276 ± 0.101	0.388 ± 0.006	0.495 ± 0.040	167.1 ± 2.1	87.9 ± 6.4
28	Nep	Jup	1981 Mar 1	CH3	0.830 ± 0.042	0.372 ± 0.006	0.309 ± 0.016	165.5 ± 2.5	63.3 ± 2.5
29	Nep	Jup	1981 Mar 1	CH4	1.191 ± 0.178	0.372 ± 0.006	0.443 ± 0.067	134.6 ± 4.5	67.5 ± 8.4
30	Nep	Jup	1981 Mar 1	CH5	1.128 ± 0.151	0.372 ± 0.006	0.420 ± 0.057	167.1 ± 2.1	76.1 ± 9.0

[a] Filter y is CH2 in every case.

[b] S(ax)/S(ay) = ratio of signal from planet a with filter x (column 4) to signal from planet a with filter y (CH2), etc. The signal ratios have been corrected to 1 mm line-of-sight water vapor for filters CH2, CH3, CH4, NO4, and CH5, and to 5mm line-of-sight water vapor for MP2. The corresponding wavelengths are 414, 353, 450, 517, 664(1mm), and 938(5mm).

[c] B(ay) = brightness of planet a with filter y, etc. The values of the brightness ratios are taken from Table II column (14) using data from the same dates except as otherwise noted (footnote f).

[d] Column (5) times column (6).

[e] Assumed brightness temperature of planet b, filter x based on Wright's model (see Section III of text), where planet b is Mars, and on the results shown in Table V, where planet b is Jupiter.

[f] Average of earlier data on B(ay)/B(by) for same planets with error multiplied by 3. (No direct measurement of B(ay)/B(by) on February 22.)

[g] Average of values for same planet and filter.

TABLE IV

JOURNAL OF OBSERVATIONS: AIRBORNE DATA

Line	(1) Planet a	Planet b	(3) Date (UT)	(4) Filter (Aperture)	(5) (6) r.m.s H_2O[a] w(a) (μm)	w(b) (μm)	(7) Signal Ratio[b]	(8) (9) Semi-diameter a(a) (arc sec)	a(b)	(10) (11) Finite Disk correction D(a)	D(b)	(12) λ (μm)	(13) Flux Density (Jy)	(14) Planet Temp.[c] T_b (K)
			1980											
1	Jup	Mars	May 2	G1-1(73)	6.3	6.2	4.31	19.03	4.54	1.097	1.005	38.7	1210000	134.0
2	Jup	Mars	May 2	G1-2(73)	6.3	6.1	6.69	19.03	4.54	1.097	1.005	55.1	1130000	138.5
3	Jup	Mars	May 2	G1-3(73)[f]	5.8	6.7	7.03	19.03	4.54	1.097	1.005	62.6	874000	129.0
4	Jup	Mars	May 2	G1-4(73)[f]	5.8	5.4	8.03	19.03	4.54	1.097	1.005	109.4	471000	131.5
5	Jup	Mars	May 2	G1-5(73)[f]	5.9	5.2	8.77	19.03	4.54	1.097	1.005	168.2	211000	118.8
6	Jup	Mars	May 2	S1-150(127)	6.3	6.3	8.92	19.03	4.54	1.031	1.002	135.4	330000	128.1
7	Jup	Mars	May 2	S1-200(127)	5.8	5.8	9.27	19.03	4.54	1.031	1.002	167.4	210000	117.9
8	Jup	Mars	May 2	S1-150L(127)	7.3	7.0	9.97	19.03	4.54	1.031	1.002	204.0	178000	132.7
9	Jup	Mars	May 2	S1-250(127)	6.5	5.2	10.05	19.03	4.54	1.031	1.002	221.8	156000	133.6
10	Jup	Mars	May 2	S1-250L(127)	6.9	6.6	10.41	19.03	4.54	1.031	1.002	328.6	83900	143.7
11	Sat	Mars	Jan 16	G1-1(49)	9.1	6.7	0.202	8.83	5.51	1.046	1.018	40.2	98500	99.4
12	Sat	Mars	Jan 16	G1-2(49)	9.1	6.9	0.442	8.83	5.51	1.046	1.018	56.1	113000	101.8
13	Sat	Mars	Jan 16	G1-3(49)	9.0	7.6	0.513	8.83	5.51	1.046	1.018	64.9	112000	103.9
14	Sat	Mars	Jan 16	G1-4(49)[g]	9.0	7.0	0.606	8.83	5.51	1.046	1.018	102.6	68000	99.3
15	Sat	Mars	Jan 16	G1-5(49)[g]	9.0	7.5	0.732	8.83	5.51	1.046	1.018	148.6	42500	99.9
16	Sat	Mars	Jan 16	S1-100(127)	9.0	6.8	0.668	8.83	5.51	1.007	1.003	99.4	67800	97.3
17	Sat	Mars	Jan 16	S1-150(127)	9.0	6.6	0.771	8.83	5.51	1.007	1.003	135.5	46600	97.6
18	Sat	Mars	Jan 16	S1-200(127)	9.3	6.9	0.838	8.83	5.51	1.007	1.003	168.1	33500	96.1
19	Sat	Mars	Jan 16	S1-150L(127)	9.0	6.9	0.903	8.83	5.51	1.007	1.003	205.2	25300	98.1
20	Sat	Mars	Jan 16	S1-250L(127)	9.0	6.3	1.033	8.83	5.51	1.007	1.003	331.6	12900	109.9
21	Sat	Mars	May 2	G1-1(73)	7.8	6.2	0.320	8.96	4.54	1.021	1.005	40.2	91700	96.8
22	Sat	Mars	May 2	G1-2(73)	7.6	6.1	0.728	8.96	4.54	1.021	1.005	56.2	112000	100.3
23	Sat	Mars	May 2	G1-3(73)[f]	7.5	6.7	0.870	8.96	4.54	1.021	1.005	65.9	113000	103.6
24	Sat	Mars	May 2	G1-4(73)[f]	8.4	5.4	1.20	8.96	4.54	1.021	1.005	110.8	66800	101.7
25	Sat	Mars	May 2	G1-5(73)[f]	8.1	5.2	1.38	8.96	4.54	1.021	1.005	169.3	35100	98.1
26	Sat	Mars	May 2	S1-150(127)	8.5	6.3	1.29	8.96	4.54	1.007	1.002	135.5	49900	100.0
27	Sat	Mars	May 2	S1-200(127)	8.7	5.8	1.32	8.96	4.54	1.007	1.002	168.1	33600	94.6
28	Sat	Mars	May 2	S1-150L(127)	9.3	7.0	1.44	8.96	4.54	1.007	1.002	205.2	25400	96.3
29	Sat	Mars	May 2	S1-250(127)	8.3	5.7	1.48	8.96	4.54	1.007	1.002	222.2	21600	94.1
30	Sat	Mars	May 2	S1-250L(127)	8.8	6.6	1.72	8.96	4.54	1.007	1.002	331.6	12900	106.9
31	Sat	Mars	May 13	G1-1(73)	9.3	8.1	0.361	8.81	4.17	1.020	1.005	40.2	86800	96.2
32	Sat	Mars	May 13	G1-2(73)	8.9	8.6	0.840	8.81	4.17	1.020	1.005	56.2	105000	99.4
33	Sat	Mars	May 13	G1-4(73)[f]	9.4	8.4	1.50	8.81	4.17	1.020	1.005	110.9	67200	104.0
34	Sat	Mars	May 13	G1-5(73)[f]	9.6	8.0	1.75	8.81	4.17	1.020	1.005	169.7	36600	103.4
35	Ur	Sat	May 7	G1-1(49)	11.0	11.7	0.00477 ± 20	1.98	8.90	1.002	1.046	42.8	536	59.9
36	Ur	Sat	May 7	G1-2(49)	10.4	11.7	0.00868 ± 0	1.98	8.90	1.002	1.046	57.7	924	59.6
37	Ur	Sat	May 7	G1-3(49)[f]	11.4	11.7	0.0121 ± 2	1.98	8.90	1.002	1.046	74.0	1167	60.2
38	Ur	Sat	May 7	G1-4(49)[f]	11.0	12.1	0.0184 ± 2	1.98	8.90	1.002	1.046	115.1	1075	60.1
39	Ur	Sat	May 7	G1-5(49)[f]	11.0	12.1	0.0230 ± 3	1.98	8.90	1.002	1.046	166.7	973	60.9
40	Ur	Sat	May 7	S1-150(127)	11.1	12.0	0.0198 ± 9	1.98	8.90	1.000	1.007	136.9	915	59.3
41	Ur	Sat	May 7	S1-200(127)	10.7	12.3	0.0219 ± 9	1.98	8.90	1.000	1.007	172.5	723	59.2
42	Ur	Sat	May 7	S1-150L(127)	10.4	12.2	0.0244 ± 6	1.98	8.90	1.000	1.007	211.6	594	61.2
43	Ur	Sat	May 7	S1-250(127)	10.7	12.3	0.0260 ± 8	1.98	8.90	1.000	1.007	224.1	568	62.4
44	Ur	Sat	May 7	S1-250L(127)	11.4	12.2	0.0262 ± 18	1.98	8.90	1.000	1.007	329.7	324	63.5
			1982											
45	Ur[d]	Mars[e]	May 18	G2-1(49)	11.7	13.0	9.38×10^{-4}	1.97	5.93	1.000	1.020	42.8	583	60.6
46	Ur[d]	Mars[e]	May 18	G2-2(49)	11.8	13.0	3.59×10^{-3}	1.97	5.93	1.000	1.020	57.7	934	59.5
47	Ur[d]	Mars[e]	May 18	G2-4(49)[g]	11.8	12.0	9.56×10^{-3}	1.97	5.93	1.000	1.020	115.2	990	58.4
48	Ur[d]	Mars[e]	May 18	G2-5(49)[g]	12.0	12.0	1.61×10^{-2}	1.97	5.93	1.000	1.020	166.8	803	61.7
49	Ur[d]	Mars[e]	May 18	G2-6(49)	11.8	14.0	1.04×10^{-2}	1.97	5.93	1.000	1.020	101.2	1062	58.6
50	Ur	Mars	May 18	G2-4(49)[h]	12.0	13.9	1.05×10^{-2}	1.97	5.93	1.000	1.020	115.8	878	55.7
51	Ur	Mars	May 18	G2-5(49)[h]	12.0	13.8	1.74×10^{-2}	1.97	5.93	1.000	1.020	168.8	733	59.2
52	Ur	Mars	May 18	G2-1(33)	11.8	12.0	1.02×10^{-3}	1.97	5.93	1.005	1.043	42.8	625	61.7
53	Ur	Mars	May 18	G2-2(33)	11.7	11.9	3.72×10^{-3}	1.97	5.93	1.005	1.043	57.8	958	60.2
54	Ur[d]	Mars	Aug 29	G2-1(49)	14.0	15.0	2.71×10^{-3}	1.86	3.20	1.000	1.006	42.8	494	60.4
55	Ur[d]	Mars	Aug 29	G3-2(49)	14.0	15.0	9.69×10^{-3}	1.86	3.20	1.000	1.006	57.7	740	58.3
56	Ur	Mars	Aug 29	G2-6(49)	14.0	15.0	2.62×10^{-2}	1.86	3.20	1.000	1.006	101.2	789	54.8
57	Ur	Mars	Sep 2	G2-1(49)	12.0	12.0	2.45×10^{-3}	1.86	3.15	1.000	1.005	42.8	437	59.1
58	Ur	Mars	Sep 2	G2-2(49)	12.0	12.0	9.85×10^{-3}	1.86	3.15	1.000	1.005	57.8	742	58.3
59	Ur	Mars	Sep 2	G2-4(49)[g]	12.0	12.0	2.44×10^{-2}	1.86	3.15	1.000	1.005	115.2	719	53.7
60	Ur	Mars	Sep 2	G2-5(49)[g]	12.0	12.0	4.02×10^{-2}	1.86	3.15	1.000	1.005	166.8	588	55.7
61	Nep[d]	Ur	May 16	G2-1(49)	7	7	0.408 ± 34	1.15	1.97	1.000	1.000	41.8	184	60.8
62	Nep[d]	Ur	May 16	G2-2(49)	7	7	0.369 ± 8	1.15	1.97	1.000	1.000	58.1	347	61.0
63	Nep[d]	Ur[e]	May 16	G2-4(49)[h]	7	7	0.378 ± 8	1.15	1.97	1.000	1.000	113.3	361	59.8
64	Nep[d]	Ur[e]	May 16	G2-5(49)[h]	7	7	0.355 ± 13	1.15	1.97	1.000	1.000	164.7	267	60.4
65	Nep[d]	Ur[e]	May 16	G2-6(49)	7	7	0.402 ± 15	1.15	1.97	1.000	1.000	101.1	399	60.8
66	Nep[d]	Ur	May 16	G2-1(33)	7	7	0.375 ± 22	1.15	1.97	1.000	1.000	41.8	168	59.8
67	Nep	Ur	May 16	G2-2(33)	7	7	0.366 ± 9	1.15	1.97	1.000	1.000	58.2	345	60.9
68	Nep	Ur	May 16	G2-6(33)	7	7	0.384 ± 17	1.15	1.97	1.000	1.000	99.7	382	59.7
69	Nep	Ur[e]	Aug 29	G2-1(49)	11.0	14.0	0.466	1.14	1.86	1.000	1.000	41.8	181	60.7
70	Nep	Ur[e]	Aug 29	G2-2(49)	11.0	14.0	0.420	1.14	1.86	1.000	1.000	58.0	338	60.9
71	Nep	Ur	Aug 29	G2-4(49)[g]	11.0	14.0	0.406	1.14	1.86	1.000	1.000	113.6	328	57.9
72	Nep	Ur[e]	Aug 29	G2-5(49)[g]	11.0	14.0	0.414	1.14	1.86	1.000	1.000	165.3	265	60.9
73	Nep	Ur	Aug 29	G2-6(49)	11.0	14.0	0.386	1.14	1.86	1.000	1.000	101.0	324	56.6
			1983											
74	Ur	Jup	Jun 4	H1-1(73)	13.0	12.0	.00177	1.96	21.89	1.000	1.127	105.9	1017	58.2
75	Ur	Jup	Jun 4	H1-3(73)	13.0	12.0	.00205 ± 6	1.96	21.89	1.000	1.127	137.2	798	56.3
76	Ur	Jup	Jun 4	H1-6(73)	12.0	11.0	.00270 ± 2	1.96	21.89	1.000	1.127	191.1	618	58.7
77	Ur	Jup	Jun 4	H1-7(73)	12.0	11.0	.00272 ± 2	1.96	21.89	1.000	1.127	198.2	590	58.7

[a] Line of sight water vapor based on a boresight radiometer for lines 1 to 44 and on a zenith radiometer and secant z for lines 45 to 73. On May 16 (lines 61 to 68) the zenith radiometer failed before the planet observations. A typical zenith value was used to estimate the boresight value.

[b] The errors in the least significant digits are shown in cases where repeated measurements permitted statistical error analysis.

[c] We estimate the statistical errors (not including the errors in the Mars calibration) at 1.5K for Jupiter, Saturn and Uranus, and 3.5K for Neptune.

[d] Two observations of planet a averaged.

[e] Two observations of planet b averaged.

[f] The short-wavelength blocking filter was Teflon.

[g] For these measurements filters 4 and 5 were used without any Teflon or CaF_2 for short-wavelength blocking. The data have been corrected taking into account a small measured leak at ~ 20 μm.

[h] The short-wavelength blocking filter was CaF_2.

TABLE V

BRIGHTNESS TEMPERATURES[a]

(Summary of Data from Tables II, III, and IV)

Line	Jupiter		Saturn		Uranus		Neptune	
	λ (μm)	Temp (K)	λ (μm)	Temp (K)	λ (μm)	Temp (K)	λ (μm)	Temp (K)
1	38.7	134.0	40.2	97.5 ± 1.7[b]	42.8	60.3 ± 0.7[c]	41.8	60.6 ± 0.5[c]
2	55.1	138.5	56.2	100.5 ± 1.2[b]	57.7	59.2 ± 0.7[c]	58.1	60.9 ± 0.1[c]
3	62.6	129.0	65.4	103.7 ± 0.2[b]	74.0	60.2	100.8	58.9 ± 2.1[c]
4	109.4	131.5	99.4	97.3	102.8	57.2 ± 2.1[b]	113.4	58.9 ± 1.3[b]
5	135.4	128.1	102.6	99.3	115.3	57.0 ± 2.8[b]	165.0	60.7 ± 0.4[b]
6	168.0	118.4 ± 0.6[b]	110.8	102.9 ± 1.6[b]	137.0	57.8 ± 2.1[b]		
7	204.0	132.7	135.5	98.8 ± 1.7[b]	167.3	59.4 ± 2.7[b]		
8	221.8	133.6	148.6	99.9	172.5	59.2		
9					191.1	58.7		
10					198.2	58.7		
11	328.6	143.7	168.6	97.2 ± 3.3[b]	211.6	61.2		
12			205.2	97.2 ± 1.3[b]	224.1	62.4		
13			222.2	94.1	329.7	63.5		
14			331.6	108.4 ± 2.1[b]				
15	353	165.5 ± 2.5	353	112.9 ± 1.1	353	62.4 ± 2.3	353	63.3 ± 2.5
16	414	155.3 ± 1.3	414	119.2 ± 1.2	414	70.1 ± 1.3	414	67.9 ± 1.2
17	450	135 ± 5	450	112.3 ± 3.2	450	73 ± 5	450	68 ± 8
18	517	149.9 ± 2.6	517	122.2 ± 1.1				
19	664	167.1 ± 2.1	664	137 ± 4	664	88 ± 6	664	76 ± 9
20	968	175 ± 10	968	134.5 ± 3.2	968	94.5 ± 2.3	968	103 ± 7

[a]None of the errors shown in this table includes the uncertainty in the Mars calibration. Errors for IRTF data (lines 13-18) are computed as specified in Appendix D. Errors shown for KAO data (lines 1-12) are standard deviations of two or more measurements from Table IV where the effective wavelengths fall within a range of 2 μm. (See footnotes b and c concerning weighting.) The mean of the 19 errors for KAO data is 1.5 K (see discussion in text).

[b]Average of data for bandpass and low pass filters with values of λ_{eff} within 2 μm. Bandpass measurements are given twice the weight of low pass measurements.

[c]Average of data for 33" and 49" apertures (λ_{eff} within 2 μm). To allow for possible guiding errors the 33" measurements are given half the weight of 49" measurements.

1. Report No.	2. Government Accession No.	3. Recipient's Catalog No.
NASA TM-88179		

4. Title and Subtitle	5. Report Date
FAR INFRARED AND SUBMILLIMETER BRIGHTNESS TEMPERATURES OF THE GIANT PLANETS	November 1985
	6. Performing Organization Code

7. Author(s)	8. Performing Organization Report No.
R. H. Hildebrand*, R. F. Loewenstein*, D. A. Harper*, G. S. Orton†, Jocelyn Keene* and S. E. Whitcomb*	86003
	10. Work Unit No.

9. Performing Organization Name and Address	11. Contract or Grant No.
*Ames Research Center, Moffett Field, CA 94035 †Jet Propulsion Laboratory, California Institute of Technology, 4800 Oak Grove Dr., Pasadena, CA 91109	

12. Sponsoring Agency Name and Address	13. Type of Report and Period Covered
National Aeronautics and Space Administration Washington, DC 20546	Technical Memorandum
	14. Sponsoring Agency Code 352-02-03

15. Supplementary Notes

Preprint Series #33. Supported by NASA grants.
Point of Contact: L. C. Haughney, Ames Research Center, MS 211-12, Moffett Field, CA 94035, (415) 694-5339 or FTS 464-5339

16. Abstract

We have measured the brightness temperatures of Jupiter, Saturn, Uranus, and Neptune in the range 35- to 1000-μm. The effective temperatures derived from the measurements, supplemented by shorter wavelength Voyager data for Jupiter and Saturn, are 126.8 ±4.5 K, 93.4 ±3.3 K, 58.3 ±2.0 K, and 60.3 ±2.0 K, respectively. We discuss the implications of the measurements for bolometric output and for atmospheric structure and composition. The temperature spectrum of Jupiter shows a strong peak at ~350 μm followed by a deep valley at ~450- to 500-μm. Spectra derived from model atmospheres qualitatively reproduce these features but do not fit the data closely.

17. Key Words (Suggested by Author(s))	18. Distribution Statement
Planets: giant Far-infrared: Brightness temperatures	Unlimited Subject category - 89

19. Security Classif. (of this report)	20. Security Classif. (of this page)	21. No. of Pages	22. Price*
Unclassified	Unclassified	75	A04

*For sale by the National Technical Information Service, Springfield, Virginia 22161

End of Document